BRNO UNIVERSITY OF TECHNOLOGY
VYSOKÉ UČENÍ TECHNICKÉ V BRNĚ

FACULTY OF MECHANICAL ENGINEERING
FAKULTA STROJNÍHO INŽENÝRSTVÍ

INSTITUTE OF PHYSICAL ENGINEERING
ÚSTAV FYZIKÁLNÍHO INŽENÝRSTVÍ

FABRICATION AND CHARACTERIZATION OF ATOMICALLY THIN LAYERS
PŘÍPRAVA A CHARAKTERIZACE ATOMÁRNĚ TENKÝCH VRSTEV

MASTER'S THESIS
DIPLOMOVÁ PRÁCE

AUTHOR — **Bc. Jan Tesař**
AUTOR PRÁCE

SUPERVISOR — **Ing. Pavel Procházka, Ph.D.**
VEDOUCÍ PRÁCE

BRNO 2020

BRNO UNIVERSITY OF TECHNOLOGY
FACULTY OF MECHANICAL ENGINEERING

Specification Master's Thesis

Department:	Institute of Physical Engineering
Student:	**Bc. Jan Tesař**
Study programme:	Applied Sciences in Engineering
Study field:	Physical Engineering and Nanotechnology
Supervisor:	**Ing. Pavel Procházka, Ph.D.**
Academic year:	2019/20

Pursuant to Act no. 111/1998 concerning universities and the BUT study and examination rules, you have been assigned the following topic by the institute director Master's Thesis:

Fabrication and characterization of atomically thin layers

Recommended bibliography:

DEAN, C. R., YOUNG, A. F., MERIC, I., et al. Boron nitride substrates for high-quality graphene electronics. Nature Nanotechnology. 2010, 5(10), 722-726.

WANG, J., MA, F. and SUN, M. Graphene, hexagonal boron nitride, and their heterostructures: properties and applications. RSC Advances. 2017, 7(27), 16801-16822.

TAN, Ch., CAO, X., WU, X. J., et al. Recent Advances in Ultrathin Two-Dimensional Nanomaterials. Chemical Reviews. 2017, 117(9), 6225-6331.

Deadline for submission Master's Thesis is given by the Schedule of the Academic year 2019/20

In Brno,

L. S.

prof. RNDr. Tomáš Šikola, CSc.
Director of the Institute

doc. Ing. Jaroslav Katolický, Ph.D.
FME dean

ABSTRACT

This work is focused on the area of two-dimensional materials, their preparation, and analysis. Probably the most known representative of two-dimensional materials is the graphene. This 2D carbon allotrope, sometimes called the "father of 2D materials", offers an intriguing combination of electrical, thermal, and mechanical properties. Graphene received a lot of attention and has been prepared by many approaches. Still, one preparation method stands superior in the meaning of graphene quality. Mechanical exfoliation is very simple in comparison to other techniques that still produces graphene of the highest quality.

The thesis is also focused on the optimization of the process producing heterostructures based upon graphene and hBN layers. The established process yielded multiple van der Waals heterostructures, which were analyzed by Raman spectroscopy, atomic force microscopy, and low electron energy microscopy. The charge carrier mobility measurements were also accomplished at the GFET setup. Obtained values of mobility demonstrated excelling transport properties of the exfoliated graphene over the graphene prepared by other methods. Thus proving the described creation process as suitable for the preparation of quality heterostructures.

KEYWORDS

Graphene, hBN, SiO_2, 2D materials, van der Waals heterostructures, mechanical cleavage, GFET, charge carrier mobility

ABSTRAKT

Tato práce se zabývá oblastí dvourozměrných materiálů, jejich přípravou a analýzou. Pravděpodobně nejznámějším zástupcem dvourozměrných materiálů je grafen. Tento 2D allotrop uhlíku, někdy nazývaný „otec 2D materiálů“, v sobě spojuje neobyčejnou kombinaci elektrických, tepelných a mechanických vlastností. Grafen získal mnoho pozornosti a byl také připraven mnoha metodami. Jedna z těchto metod však stále vyniká nad ostatními kvalitou produkovaného grafenu. Mechanická exfoliace je ve srovnání s jinými technikami velmi jednoduchá, takto připravený grafen je však nejkvalitnější.

Práce je také zaměřena na optimalizaci procesu tvorby heterostruktur složených z vrstev grafenu a hBN. Dle prezentovaného postupu bylo připraveno několik van der Waalsových heterostruktur, které byly analyzovány Ramanovskou spektroskopií, mikroskopií atomových sil a nízkoenergiovou elektronovou mikroskopií. Měření pohyblivosti nosičů náboje bylo provedeno v GFET uspořádání. Získané hodnoty pohyblivosti prokázaly vynikající transportní vlastnosti exfoliovaného grafenu v porovnání s grafenem připraveným jinými metodami. V práci popsaný proces přípravy je tedy vhodný pro výrobu kvalitních heterostruktur.

KLÍČOVÁ SLOVA

Grafen, hBN, SiO_2, 2D materiály, van der Waalsovy heterostruktury, mechanická exfoliace, GFET, pohyblivost nosičů náboje

TESAŘ, Jan. *Fabrication and characterization of atomically thin layers*. Brno, 2020, 67 p. Master's Thesis. Brno University of Technology, Faculty of Mechanical Engineering, Institute of Physical Engineering. Advised by Ing. Pavel Procházka, Ph.D.

Typeset by the `thesis` package, version 4.00; `http://latex.feec.vutbr.cz`

DECLARATION

I declare that I have written the Master's Thesis titled "Fabrication and characterization of atomically thin layers" independently, under the guidance of the advisor and using exclusively the technical references and other sources of information cited in the thesis and listed in the comprehensive bibliography at the end of the thesis.

As the author I furthermore declare that, with respect to the creation of this Master's Thesis, I have not infringed any copyright or violated anyone's personal and/or ownership rights. In this context, I am fully aware of the consequences of breaking Regulation § 11 of the Copyright Act No. 121/2000 Coll. of the Czech Republic, as amended, and of any breach of rights related to intellectual property or introduced within amendments to relevant Acts such as the Intellectual Property Act or the Criminal Code, Act No. 40/2009 Coll., Section 2, Head VI, Part 4.

Brno ....

author's signature

ACKNOWLEDGEMENT

I would like to kindly thank my supervisor Ing. Pavel Procházka Ph.D. for careful guidance and professional comments during the entire elaboration of this master's thesis. I would like to express my gratitude to all, who helped me to complete this work and encouraged me when times were uncertain. Especially to my dearest classmates how held my spirit up with never-ending humor and support especially during the last days of work. CzechNanoLab project LM2018110 funded by MEYS CR is gratefully acknowledged for the financial support of the measurements/sample fabrication at CEITEC Nano Research Infrastructure. At last, I cannot thank enough my family, without them this thesis would not be achieved at all.
To everyone involved in this work – I do thank you very much.

Contents

List of Figures

Introduction

The area of two-dimensional materials represents a relatively new field of research which has provided a number of interesting discoveries. Two-dimensional materials include many already known materials in their less-known form. Materials made of atomically thin layers are present in nature like Kaolinite, the clay mineral. Other thin films could be completely synthesized, e.g. 2D form of silicone – the silicene. 2D materials can be also combined to create new structures, usually bonded via weak inter-layer interaction, the van der Waals heterostructures. Section 1.2 *2D Materials* deals with this topic.

Yet, probably the most known representative of two-dimensional materials is the graphene. This 2D carbon allotrope is often called "father of 2D materials". Carbon, as one of the most abundant elements in the universe, is found in many forms. Diamond, graphite, spherical fullerenes, or tubular-shaped carbon nanotubes – they all have one thing in common: they are all based on carbon atoms arranged in a hexagonal shape, based on graphene. Section 1.1 *Carbon Allotropes* describes these carbon forms except graphene itself, which has it own subsection 1.2.1.

Graphene offers an intriguing combination of electrical, thermal, and mechanical properties. Graphene is five times stronger (graphene has Young's modulus five times greater) than construction steel, has thermal conductivity ten times higher than copper, is transparent in the visible spectrum, and is an exceptional electronic conductor. All of this originates in strong covalent bonds between the carbon atoms, stable hexagonal crystal structure, one-atom thickness, and an interesting linear dispersion relation near the zero carrier concentration, called Dirac point.

Such properties dragged a lot of attention, and graphene has been prepared by many approaches that utilize various growth precursors. Decomposition of gaseous hydrocarbons on metals and temperature-induced solubility change are some of the principles which were used for the graphene growth in the past. Yet, one preparation method still stands superior in the meaning of graphene quality. Mechanical exfoliation is very simple in comparison to other techniques, more details in section 1.3. Graphene could be prepared by exfoliation even at home, the only needed tools are graphite and adhesive tape. Nevertheless, properties that attracted the world-wide attention of the scientific community were mostly presented on the exfoliated graphene.

The graphene of the highest quality is still relevant for the continuing research. This work is focused on the optimization of the process producing heterostructures based upon such graphene layers and their analysis by various methods as *Experimental part* describes.

1 Theoretical part

The first part of this thesis is devoted to the theoretical background of this work. The first chapter – *Carbon allotropes* describes not just graphene, which is in the center of this work, but also other structurally different forms of carbon like the diamond, graphite, fullerenes, and others. For a main forms of carbon, the preparation techniques and applications are described. Graphene has its own chapter devoted to the history, properties, and application of this material. One chapter is devoted to other two-dimensional materials like hexagonal boron nitride, molybdenum disulfide, and others. The chapter *Preparation of 2D materials* focuses on methods like chemical vapor deposition, mechanical exfoliation, or epitaxial growth, which are commonly used for the growth of before mentioned 2D materials. One chapter is focused on how the substrate affects the graphene properties and the other one on the charge carrier mobility.

Further chapters are devoted to analytical methods and preparation techniques used during the realization of this work like exfoliation, Raman spectroscopy, EBL, and LEEM. The last chapter is about measuring setup. The details about each step that was made for this work are detailed in the second main part of the thesis the *Experimental part*.

1.1 Carbon Allotropes

The 6th element of the periodic table noted as "C" is carbon, an element which can form stable chemical bonds with many other elements and is also the basis of life. Carbon is one of the most abundant element in the universe, on the Earth, and it is found almost everywhere. Every living organism is build from organic compounds based on carbon-carbon bonds.

As an element, carbon is able to create a wide range of structures. Materials that consist of the same atoms, but are arranged in a different configuration are called allotropes. The different chemical bonds or crystallographic structures of carbon atoms lead to different properties in such a way that one may say these materials are unrelated. As explanatory example can be given comparison of a diamond and and a graphite. Both are made of carbon atoms, yet diamond is the hardest mineral and graphite is so soft that it is used for drawing.

Carbon atoms are capable of creating three hybridizations. The most common one is sp^3 hybridization, where every carbon atom is bonded to four other atoms with a single covalent bond. Such a hybridization can be found in 3D carbon form like a diamond. The hybridization sp^2 is to be found in graphite, in which is every carbon atom connected via single covalent bond to three other atoms. The last hybridization of which is carbon capable is sp. This hybridization is the base of a 1D carbon chain called "carbyne" in where is every atom connected to the other via one single and one triple covalent bond or two double covalent bonds. The different carbon hybridizations and schematic representation of involved electron orbitals may be seen in Fig. 1.1.

The following paragraphs describe properties, differences, and on the other side, the similarities between the wide range of carbon allotropes, besides diamond and graphite, carbon chains, fullerenes or nanotubes.

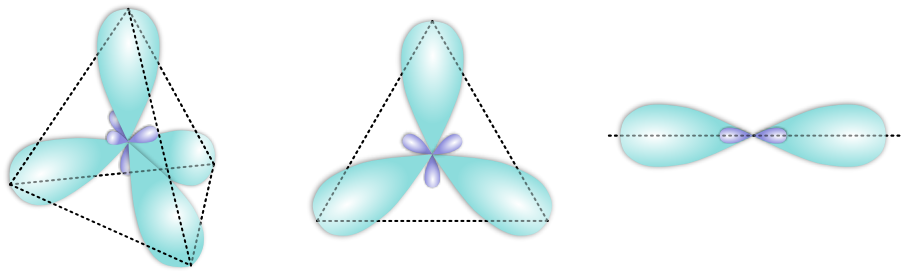

a) sp^3 b) sp^2 c) sp

Fig. 1.1: Comparison of different carbon orbital hybridizations. (a) 3D tetrahedral sp^3, (b) 2D triangular sp^2 and (c) 1D linear sp hybridization.

1.1.1 Diamond

One of the most known forms of carbon is diamond. Carbon atoms are arranged in a variation of a face-centered cubic crystal structure. Diamond is one of the hardest minerals known to man. It is ranked as 10 at Mohs scale of mineral hardness and it is four times harder than corundum, which is ranked as 9. Similar hardness to diamond could be found in a boron nitride, which has the same structure, but instead of carbon, the boron and nitrogen atoms are present. Diamond has a strong and stable 3D structure of covalent bonds between the carbon atoms, which all have sp^3 hybridization. Every atom is connected to another three atoms within the structure of tetrahedron. Diamond's structure contains carbon atoms in hexagonal shape as well as the graphite or graphene do. The diamond structure could be seen in Fig. 1.2.

Diamond, as the only precious stones can have all colored modifications thanks to a small number of impurities. For example, the yellow color is due nitrogen, blue due boron, brown thanks to defects and green because of exposure to radiation. the unit of weight of a diamond is the carat and it's defined as $1\,\mathrm{ct} = 0.2\,\mathrm{g}$. The usual weight of diamonds on the jewelry market is in hundredths, tenths to units of carats.

Diamond has a wide bandgap of 5.5 eV and it is an excellent electric insulator. However, some blue diamonds which contains boron atoms are natural semiconductors because boron impurities are donating a hole into valence band [1]. The diamond is transparent within infrared, visible, and ultraviolet wavelengths thanks to a wide bandgap which corresponds to 225 nm.

One of the properties of diamond is high chemical stability. Diamond does not react with any strong acid nor base at room temperature. However, diamond ignites around 750 °C at pure oxygen atmosphere and burns at the pale blue flame and continues after removing the source of heat. Such a scenario can not be done in the air atmosphere because the concentration of oxygen is not high enough.

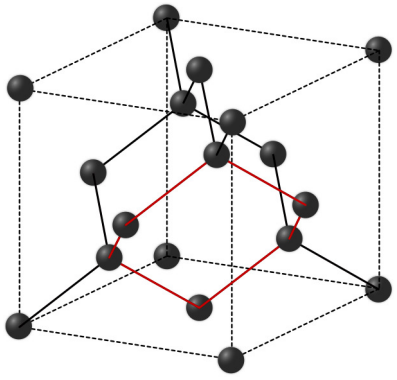

Fig. 1.2: Atomic structure of diamond crystal. Carbon atoms are arranged in hexagonal shape as illustrated with red lines.

1.1.2 Graphite

Another well-known carbon allotrope is graphite. This crystalline form of carbon is yet another natural mineral which may be in a form of flakes or even in a form of very small flakes - amorphous graphite. Hexagonal lattice describes the crystal structure of graphite. Graphite consists of graphene sheets with sp^2 orbital hybridization bonded in between the graphene sheets via van der Waals bonds. Details about the crystallinity of graphene will be discussed in one of further sections. The van der Waals interaction between the graphene sheets is 0.335 nm longer. The covalent bond between the carbon atoms within the graphene sheet is 0.142 nm long as depicted in Fig. 1.3. Weak interaction between the planes is responsible for easy separation of planes, thus making graphite very soft with a hardness of 1.5 of the Mohs scale. This feature of graphite could be also used for its exfoliation to obtain graphene, as will be discussed in further sections too. Graphene is electrically conductive mainly within the plane of graphene layers.

Graphite has many similar properties to a diamond. For example, the melting point of graphite is above 3925 °C, similar to a diamond (4225 °C). Graphite is highly inert to a wide range of chemicals. Yet, like a diamond, graphite burns in an oxygen atmosphere at temperatures above 700 °C. Graphite has also some differences compared to diamond, like different hardness, electrical properties, color, or the fact that graphite is a very good lubricant while diamond is the very opposite. Graphite has also lower density of 2.26 g/cm^3 then diamond (3.51 g/cm^3) because of relatively large space in between the planes.

Graphite has a wide range of use and many applications in a variety of areas of the industry thanks to its properties like thermal stability, electrical and thermal conductivity, self-lubrication, or resistance to neutron radiation. Graphite is used in carbon microphones, lubricants, batteries, moderator rods and reflector components in nuclear reactors, steel-making, parts of wind turbine generators, ladles for liquid steel, or just pencils among other applications.

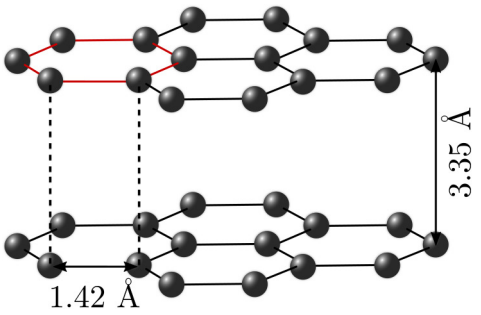

Fig. 1.3: Graphite consist of atom-thin layers made of carbon atoms in hexagonal shape – graphene. Atom within the plain are bonded via strong covalent bonds. The interaction between the layers is much weaker thus being suitable for layers delamination.

1.1.3 Fullerene

The first and most known member of fullerene class is the C_{60} molecule which was discovered by Harold Kroto, Richard E. Smalley, and Robert F. Curl in 1985 [2]. This carbon allotrope consists of 60 carbon atoms in the shape of truncated icosahedron a polygon with 60 vertices and 32 faces of which 20 are hexagonal and 12 pentagonal as can be seen in Fig. 1.4. C_{60} molecule was firstly created by laser-induced vaporization of the surface of the graphite disk surface under the flow of helium. Fullerenes are named after the American architect Buckminster Fuller, who used a similar structure for his buildings.

In a way, carbon nanotubes could be considered a special form of fullerenes. Electrons of C_{60} molecule are not shared over the whole area of the molecule, C_{60} has not superaromaticity or even aromatic character [3]. Compared to before mentioned carbon forms, the fullerenes are stable but quite reactive. Fullerenes can be dissolved in many organic solvents and can create many chemical compounds [4]. Fullerenes can be also pressed under high temperature to create C_{60} based mineral called fullerite [5] but no liquid phase of fullerenes has been observed yet. Fullerenes sublime near 425 °C without forming liquid phase [6]. Under the atmospheric pressure C_{60} forms soft crystals a weak van der Waals interaction in between C_{60} molecules with a density of about $1.6\,\mathrm{g/cm^3}$.

The prominent application of fullerenes is in biology and medicine due to their chemical properties. Fullerenes may be used as multifunctional materials for applications in tissue engineering, molecular imaging, therapeutics, drug delivery, magnetic resonance imaging, or as X-ray imaging contrast agent [7].

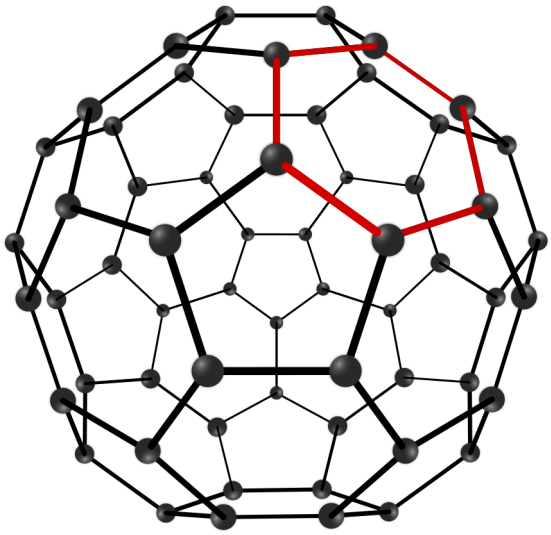

Fig. 1.4: Structure of C_{60} molecule, the most known member of the fullerenes. This carbon allotrope consists of 60 carbon atoms in a structure made of 20 are hexagons and 12 pentagons.

1.1.4 Carbyne

A less known form of carbon atoms is the 1D carbon allotrope – carbyne. Atom within carbyne are bonded via covalent bonds with only orbital hybridization sp^1. This 1D carbon chain can be connected by double bonds between every atom or with one triple and one simple bond as Fig. 1.5 shows. The problem with exploring its properties is carbyne instability in ambient conditions. One of the solutions was presented in 2006 when long carbyne linear chains were analyzed inside double-walled carbon nanotubes grown by metal-catalyzed alcohol-based CVD at high temperature and vacuum. Carbynes prepared by such a method had more than 6000 atoms within one chain [8].

Carbyne has great surface area due to the fact it is one atom thick chain and in a combination with other molecules, it might be suitable material for energy storage. For example, one study of carbine-polysulfide material suggests it as a novel cathode material and the material with a high capacity for rechargeable magnesium batteries [9]. Interesting about carbyne is its tensile stiffness which may be two times greater than tensile stiffness of graphene according to atomistic simulations [10]. Such a property could be interesting for a wide range of composite material applications, nanomechanics, or microelectromechanical systems. Carbyne can be also used in the field of bioengineering and biomaterials thanks to its high biocompatibility.

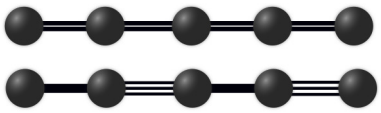

Fig. 1.5: Carbyne is the linear allotrope of carbon. The Fig. shows its structure and bonds which may be presented. The first form is bonded only via double bonds the other with one triple and one single bond.

1.1.5 Carbon nanotubes

One of the earlier mentions of carbon nanotubes (CNTs) is from the year 1975 when T. Koyama presented "carbon fibers" figures and its analysis from transmission electron microscope (TEM) [11]. Presented CNTs varied at length, diameter, and thickness yet some of which were single-walled. Carbon nanotubes are 1D macro-molecular carbon allotrope. Their diameter can be less than 1 nm, and length over 50 cm. Such a long CNTs required the CVD method with a specialized moving furnace system [12]. CNTs can be seen as a rolled graphene sheet. This is also presented in the bonding between the carbon atoms which is sp^2 orbital hybridization just like in an example of graphene – schematic structure of carbon nanotube is showed in Fig. 1.6. CNTs exhibit a very high Young's modulus with a value of around 1 TPa [13]. CNTs are good conductors, can be doped and functionalized, exhibit capillary effect, and are stable at high temperatures. Still one of the most interesting properties of CNTs is their thermal conductivity which ranges between 600 to 2000) $\mathrm{Wm^{-1}K^{-1}}$ at the room temperatures. Such a values even surpass the thermal conductivity of graphene more than 10 times [14]. CNTs are highly anisotropic when comparing thermal conductivity along the main axis and the perpendicular axis.

CNTs could be prepared on a large scale by a CVD method with metal nanoparticles or metal-hydrocarbon as a growth catalyst and a hydrocarbon or a carbon oxide as a precursor [15, 12, 16]. The alternative to this kind of method can be microwave heating technique which can be performed with or without the metal catalyst. The precursor for CNTs was ferrocene, this organometallic compound was heated up in a standard microwave oven in a vacuum [17]. Another preparation technique is utilizing electric-arc. The mixture of metallic catalysts and graphite powder is transformed with arc discharge to carbon nanotubes under inert atmosphere [18].

Carbon nanotubes could be applied in a wide range of fields like energy storage, medicine, composites materials, and many others.

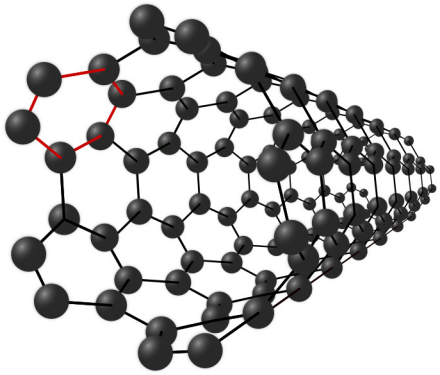

Fig. 1.6: It can be looked on a carbon nanotubes as a rolled sheet of a graphene. This describes the character of bonds between the carbon atoms and the honeycomb crystalline structure of atoms, as red color outlines. CNTs are excellent thermal conductors along the main axis.

1.1.6 Amorphous carbon

Amorphous carbon is a big class of many carbon forms that does not have a crystal structure. This class consists of charcoal, carbon black, coke, and others. Other carbon allotropes might be created by a transformation of amorphous carbon because amorphous carbon does not pose any crystalline form yet it is made of carbon atoms.

Amorphous carbon can be transformed to diamonds using nanosecond laser creating a highly under-cooled state, from which various forms of a diamond can be formed upon cooling. This process does not need for catalysts and hydrogen to obtain stabilization of the sp^3 orbital hybridization. Such a process could be executed at room temperature in the air at the atmospheric pressure resulting in the diamond crystal in the size range greater than 100 nm [19].

One research group managed to transformed amorphous carbon to graphite within 5 minutes by microwave heating. For this experiment, the graphitization of amorphous carbon powder was achieved using $NiCl_2$ as a precursor for nickel particles which worked as a metal catalyst. The powder mixture was heated at temperatures above 1000 °C using microwave radiation. Graphite was formed during the cooling of the created Ni-C alloy because the higher solubility of carbon in nickel is above 1300 °C [20].

Using the basis of the reactive empirical potential and molecular dynamics method a complete transformation of amorphous carbon clusters into fullerenes within 1 μs was done at a temperature of 2226 °C. The transformation has two stages. At the first stage, a hollow shell with sp^2 structure with attached chains is formed within 100 ns. Then, during the second stage, the carbon chains are inserted in the hollow sphere, thus creating complete fullerene in less than 1 µs [21].

Amorphous carbon could be transformed into the graphene as well. For example, utilizing thermal nickel catalyzed annealing, where during the cooling carbon atoms are precipitating through the nickel on its surface as the solubility limit is reached and are crystallizing into the graphene layer. Graphene prepared in such a way has a quality similar to other graphene growing methods [22]. More details about preparation and graphene itself will be in the following chapter dedicated to this 2D material.

1.2 2D Materials

All of the before mentioned 3D carbon allotropes have one in common. All of them have carbon atoms in hexagonal shape element within their structure as is highlighted with red color in Figs. 1.2, 1.3, 1.4, and 1.6. Carbon atoms in such an arrangement are the very base of graphene. Following this logic, one may say that the graphene (2D material) is the base of many other 3D carbon materials.

Year 2004 stands as a milestone for the field of 2D materials because of the article by the scientists Novoselov and Geim [23] which characterizes graphene and explores of some of its properties. Thanks to its extraordinary properties, graphene attracted a lot of attention from the scientific community (as Fig. 1.7 shows) and thus started an interest in other atomically thin materials – 2D materials.

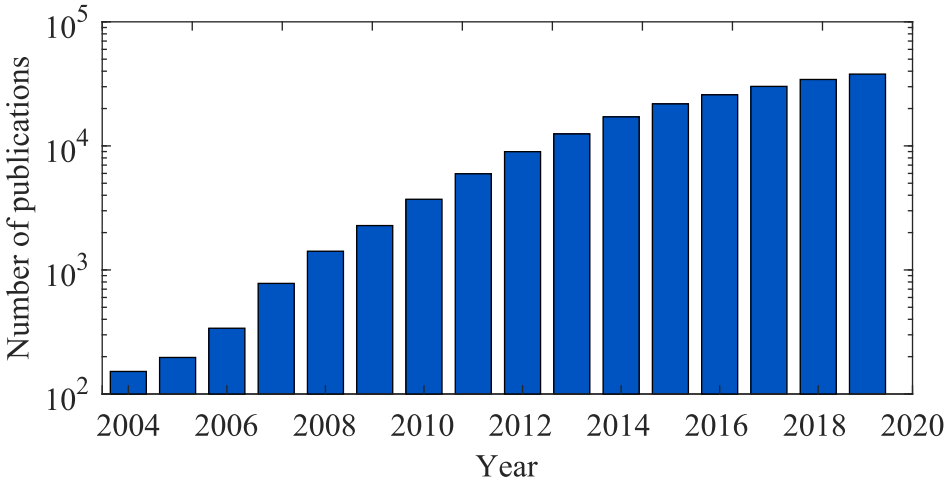

Fig. 1.7: The number of publications related to graphene per year. Two important years for the graphene and the field of 2D materials are 2004 - Geim and Novoselov's article about graphene, and 2010 - Nobel price in Physics for their work with the graphene. Thomson Reuters Web of Science (searching for graphene in topics).

1.2.1 Graphene

Carbon, as described before, can form many allotropes, many of which are out of the framework of this thesis. Graphite is a 3D crystallographic form of carbon, carbon nanotubes and carbyne are 1D form and fullerenes are a 0D form of carbon. As mentioned before, one may say all of these materials are made of the same building element the 2D carbon sheet - the graphene. An important year within the graphene and 2D material field is 2004, when researchers Andre Geim and Konstantin Novoselov analyzed the atom-thin layer of carbon atoms at the University of Manchester [23] for which they later received Nobel price in Physics in 2010. Yet, graphene was studied decades before that, earlier publications exist. The examples are: the patent for exfoliation of thin graphite sheets from 2003 [24], the study about absorption on very thin carbon layers from 1962 [25] or the first unintentional observation of graphene by transmission electron microscopy in 1948 [26]. The structure of graphene (as a part of graphite) was known many years before the graphene "rediscovery" in 2004.

Graphene is only one atom layer thin and consists of carbon atoms arrayed in a shape of a 2D hexagonal lattice. Its structure is characterized by two types of C–C bonds (σ and π) constructed from the four valence orbitals ($2s$, $2px$, $2py$, $2pz$), where the z-direction is perpendicularly out of the plane. Carbon atoms are joined by three σ-bonds to its three neighbors, these covalent bonds are quite strong (Fig. 1.8 a)). The basis of graphene consists of two bonded carbon atoms situated in the rhombus-shaped unit cell. The length between these atoms is 1.42 Å (Fig. 1.8 b)).

The bonding between the layers is mediated via weak van der Waals interaction. The electronic properties of graphene, graphite, and carbon nanotubes are determined by the bonding π- and antibonding π^*-orbitals that form wide electronic valence and conduction bands. The π-band overlapping disappears as graphene layers separate. That leads to graphene description as zero-gap semiconductor or as semi-metal. The first graphene Brillouin zone (1BZ) has also hexagonal symmetry with three main points (Fig. 1.8 c)). The K points in the vertices of 1BZ are crucial for the electronic properties of graphene. The π-band electron dispersion for graphene near the K points is found to be linear and forms so-called Dirac cones. These cones touch at the Dirac points at the Fermi level energy. The linear electronic band dispersion (Fig. 1.8 d)) leads to the unusual behavior of free charge carriers in the graphene. Electrons and holes can propagate at $\sim 1/100$ of the speed of light as massless Dirac fermions [27].

The strong bonds, 2D structure, and atypical charge carriers dispersion leads to many interesting properties of graphene.

Properties of Graphene

Graphene could potentially be useful in many field industry thanks to the properties which it exhibits. It is the superior combination of such properties in one material which draws attention to many research groups all around the world.

Mechanical properties of graphene are one of the reasons why is this material so well known. Graphene is one of the the strongest materials on Earth due to its tensile strength and Young's modulus which is 1 TPa [29]. To compare such a value, usual construction material, steel, has Young's modulus 5 times smaller. This graphene strength measurement has been conducted via AFM using mechanically exfoliated graphene flake suspended over open holes patterned in a SiO_2/Si substrate.

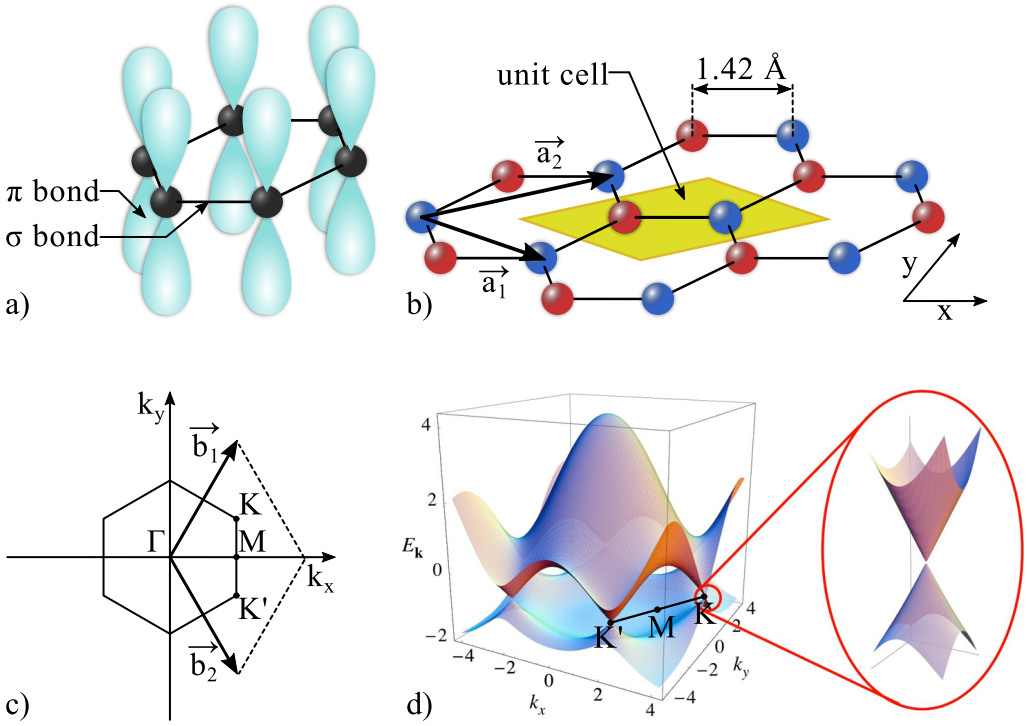

Fig. 1.8: Schematic illustration of a) bonds within carbon atoms in graphene are mediated via σ-bonds. On the other hand, the π-bonds, which are perpendicular to the graphene sheet are responsible for the delocalized system of free π-electrons, and electronic properties of graphene. b) The basis of graphene consists of two bonded carbon atoms (the red and the blue atom) situated in the rhombus-shaped unit cell (yellow area) made of two crystallographic vectors a_1 and a_2. The length between these atoms is 1.42 Å. c) The first Brillouin zone (1BZ) of graphene in reciprocal space has also a hexagonal shape with three important points due to shape symmetry. Γ point in the center of 1BZ K points in the vertices of 1BZ, and M points which are situated in the middle of its sides. d) These points are important for the graphene dispersion function of electrons because so-called Dirac points are located at the K points. The linear part of the dispersion function is depicted in the detail. This part of the dispersion is called Dirac cones. Fig. d) originally from [28] and edited.

Graphene **optical properties** are related to its thickness. Being one atom thick graphene has transmittance of 97.4 % for a light of wavelength 550 nm and with each additional layer, the light transmittance descends with the step of $\sim$ 2.3%. The minimum of transmittance in a range of wavelengths $200 - 1000$ nm is around 275 nm [30]. Graphene might be analyzed using many techniques, one of which is simply optical contrast on a substrate. The most used substrate for this analysis is SiO_2 layer on silicon substrate where graphene could be easily distinguished from few-layered graphite as Fig. 1.9 shows.

Thermal properties of graphene are anisotropic. The thermal conductivity of graphene is very high along the plane and is relatively low for out of the plane direction. The value of thermal conductivity is strongly affected by the interaction with sample surroundings, defects of lattice and further, it depends on the size of the measured sample due to the large phonon mean free path. Thermal conductivity is dominated by phonons, electron contribution is negligible as a result of a low density of charge carriers in non-doped graphene [31].

The reported in-plane thermal conductivity ranges from 2600 $Wm^{-2}K^{-1}$ for graphene grown by chemical vapor deposition (CVD) and suspended on a Au-coated SiN_x porous membrane [32] up to 5100 $Wm^{-2}K^{-1}$ for graphene obtained by mechanical exfoliation suspended over a trenches in SiO_2/Si substrate [33]. However, as mentioned before, thermal conductivity strongly depends on sample surroundings. This value for exfoliated graphene suspended by SiO_2/Si substrate is around 600 $Wm^{-2}K^{-1}$ [34]. All of before cited values of thermal conductivity were measured at room temperature. And again, to compare thermal properties of graphene, a typical metal used as a thermal conductor - copper has a thermal conductivity less than 10 times lower then graphene has.

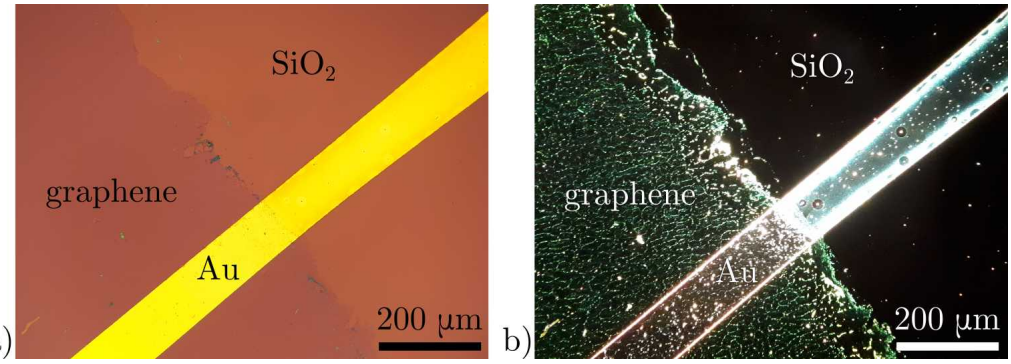

Fig. 1.9: Optical microscope images of graphene layer on SiO_2 with golden electrodes. a) Bright field and b) dark field shows the contrast of graphene on SiO_2. Graphene layer has absorption only 2.3%. However, the contrast between the clean SiO_2 area and the graphene covered area is visible thanks to light interference at the 285 nm thick SiO_2 layer. Depicted graphene sample was prepared with a chemical vapor deposition method but the effect is the same for the exfoliated graphene layers. CVD graphene shows many defects that could be seen in the dark field.

Chemical properties of graphene are prevailed by its surface in a form of large sheet and by its edges if in form of nanoribbons. Ideal graphene is mostly unreactive due to its strong covalent bonds but its reactivity with other substances could be enhanced via the functionalization process. The chemical reactivity of graphene analyzed via the D/G-peak ratio in Raman spectra of exfoliated graphene on SiO_2/Si substrate showed that edges of graphene are at least two times more reactive than its surface of the graphene sheet. The study also showed that the reactivity of single-layer graphene is almost 10 times greater than the reactivity of bi- or multi-layer graphene [35].

One way to functionalize graphene is a simple and efficient process based on nitrene chemistry. Functionalized graphene is produced from graphene oxide after a one-step reaction. Many functionalization groups could be covalently and stably anchored on graphene to modify it, for example, bromine, hydroxyl, or polystyrene. Functionalized graphene is still electrically conductive and easily dispersed in a solvent and can be processed for further applications or additional modifications [36].

Electronic properties of graphene were in a center of the study of K. Novoselov and A. Geim which afterward lead to a Nobel prize in Physics 2010. Graphene demonstrates a strong ambipolar electric field effect with zero band gap region and symmetric linear dispersion relation near the zero carrier concentration called Dirac cone. The channel conductivity may be electron or hole based on the value of the gate voltage at the field-effect transistor (FET) setup [23]. Graphene behaves as semimetal and exhibits ballistic 2D electronic transport at a long mean free path exceeding micrometer length at room temperatures [37].

In-situ annealed mechanical exfoliated graphene suspended on SiO_2/Si substrate at very low temperatures (nearly ideal conditions) exhibits charge carrier mobility over $200,000\,\mathrm{cm^2V^{-1}s^{-1}}$ as reported by [38]. The theory suggests that such a value of charge carrier mobility might be measured even at room temperatures due to weak temperature dependence and weak electron-phonon interaction in ideal bi- and mono-layer graphene [39].

It should be noted, that many of the before described properties have been reported and measured on defect-free single-layer graphene. In general, the properties of graphene with defects or other imperfections (introduced by preparation method and extrinsic effects like impurities) tend to be not so superb as just detailed in previous paragraphs. Yet, many industries could still benefit from applications of not-perfect graphene in its products.

Application of Graphene

Many interesting and superior properties could be found in graphene when compared to other material. Hence, it is not surprising that graphene is in the focus of many research groups which have found many potential applications of this 2D material.

One of the approaches of taking advantage of graphene properties are the composite materials. Graphene–polymer composites are a large group of materials with different properties with a focus on thermal stability, conductivity, or mechanical strength are investigated. The attributes of such a composite depend not only on the graphene quality but also on bonding between the filler (graphene) and the matrix (polymer), the ratio between them, or dispersity of the graphene in the polymer. For example, a composite made of flakes of functionalized graphene oxide integrated into polyelectrolyte showed improvement in mechanical properties. Its Young's modulus was enhanced from 1.5 GPa by an order of magnitude to 20 GPa with 8 vol% graphene oxide in composite [40].

Another optional application of graphene is nanoelectronics and graphene field-effect transistors (GFET). High carrier mobility, atomic thickness, and the option to change electronic properties via applied voltage are the main advantages of such devices [23]. Graphene has many times greater charge carrier mobility than silicon at room temperature. GFETs could also profit from graphene flexibility. Reusable nanosensor for blood glucose tracking was based on functionalized GFET on the polymer substrate. The device was designed to be wearable and tests showed its great durability [41]. Such an example represents graphene potential in medicine and biosensors. The drawback of the so far prepared GFET devices is the unfulfilled potential of carrier mobility (but still greater mobility than silicon has), the negative effect of high temperature on mobility, and metal-graphene contact resistance. These effects may be suppressed to some extent as shown in a study on back-gated GFETs [42].

Graphene could be also used for gas sensing applications. The reported graphene-based gas sensor for CO_2 has very high sensitivity, long device lifetime, fast response and could be easily modified to detect other gases as [43] presented. This application of graphene with additional miniaturization of the device could be useful for air quality monitoring.

Monolayered graphene oxide was used as a charge trapping medium for a memory device with a wide memory window of 7.5 V, which is important memory parameter. Memory devices based on nanocrystals usually have a memory window around 1.8 V [44]. The advantage of graphene oxide is its solubility, which can be used for easier device fabrication. Similar applications of graphene could be used in flexible organic memory devices [45].

The corrosion of metals and its alloys makes a great economic burden for the steel industry. Graphene works as an excellent barrier slowing oxygen intercalation, water, and other corrosive substances. Graphene has higher electrical conductivity than metal which causes ongoing corrosion to slow down. The drawback is the lack of methods which would produce high-quality graphene-based coating and be economically effective [46].

Photovoltaics is another area in which graphene finds its application. Perovskite solar cell with a transparent graphene electrode was reported. The cell had high

efficiency of nearly 17 %, was lightweight and low cost. This photovoltaic device had a flexible polymeric substrate, great durability, and high efficiency after 5000 bending cycles [47].

The future needs a cleaner and more efficient sources of energy like hydrogen. The large specific surface area and chemical stability are benefits of hydrogen storage devices based on graphene. Palladium nanoparticles were used as a catalyst for hydrogen sorption. The nanoporous device is charged at ambient conditions and releases hydrogen at low temperatures, the device yields a gravimetric density up to 8.67 wt.% [48].

The growth of the global population and climate changes increase demand for drinkable water. Graphene could play an important role at water purification, e.g. as a functionalized nanocomposite membrane. The reported nano-filter retained more than 99 % of organic dyes, and retained ca. 20–60 % of salts [49]. This use of graphene seems to be cost-effective because only 34 mg of material are needed for such a graphene-based membrane.

For more energy-efficient society, a proper way of energy storage is needed and a lot of attention is focused on the next-generation electrochemical energy devices. The graphene-based batteries may be the solution as [50] indicates. The reported aluminum ion battery based on microstructured graphene film cathode presented high specific capacity, high current density with more than 90 % retention 250000 charging cycles, high flexibility, and wide working temperature range.

1.2.2 Hexagonal Boron Nitride

Isomorphic 2D material of graphene made of boron and nitrogen instead of carbon is hexagonal boron nitride (hBN). This 2D material has so similar structure to graphene that some refer to it as white graphene. B and N atoms are situated in a honeycomb shape configuration with orbital hybridization sp^2. Each boron atom is bonded via a polarized covalent bond to another three nitrogen atoms. The length between the B-N atoms is 0.144 nm. Individual layers of hBN are held together by weak van der Waals interaction. The distance between planes is 0.333 nm. The schema of hBN is shown in Fig. 1.10. The hBN has such a similar crystallographic structure with graphene that their lattice constant mismatch is less than 2 % [51].

Similarly to graphene, the mechanically exfoliated hBN have high tensile stiffness. Mono-layered hBN suspended over micro-wells in Si/SiO_2 substrate exhibited Young's modulus of 0.86 TPa and fracture strength over 70 GPa, which makes hexagonal boron nitride one of the strongest electrical insulators. Interestingly, a few-layered hBN is as strong as hBN mono-layer, which is in contrast with graphene. The strength of graphene is decreasing with the number of layers. Such distinct properties seem to be caused by different interlayer interactions as the theoretical study suggests [52].

The hBN thermal conductivity was measured to be up to 280 $Wm^{-1}K^{-1}$ at room temperature, this value is comparable to the thermal conductivity of bulk hBN. Mentioned hBN was prepared by the CVD method and hBN films of different thicknesses were suspended over golden trenches on a silicon substrate. To compare, the thermal conductivity of hBN is ca. 200 times greater than thermal conductivity of SiO_2.

The area where even graphene stands behind hBN is thermal stability. Free-standing hBN prepared by Scotch tape method was exfoliated on SiO_2/Si substrate. Mono- and few-layered hBN samples went through an oxidation test in a tube furnace at different temperatures under air. The mono-layered hBN showed no effects of oxidization until 840 °C, and burned completely after 2 hours at 860 °C. Raman spectroscopy also showed no oxygen doping in hBN mono-layer until heating

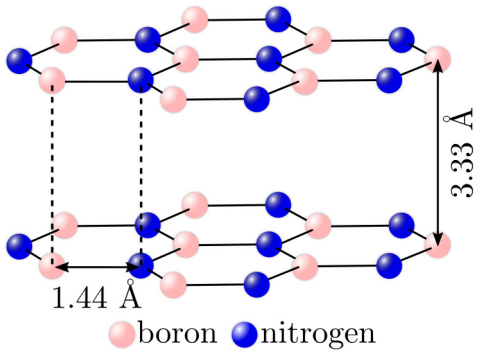

Fig. 1.10: Atomic structure of hexagonal boron nitride with corresponding crystal dimensions. hBN is structurally very similar to graphene. The lattice mismatch between these materials materials is only about 2 %.

at 700 °C in the air [53]. The adsorption of various molecules may negatively affect the final properties of nanodevices and annealing at high temperatures is one of the methods which reduce such an effect. Thus, making hBN suitable for such processes.

The properties of hBN might be useful for applications where good thermal dissipation is needed. The combinations of high thermal stability and mechanical strength could be suitable for various hBN based composite materials or various nanodevices.

Hexagonal boron exhibits outstanding chemical stability, and is also an electrical insulator, thus having even better anti-corrosion properties than graphene in the long term. The corrosion of copper foil was observed in the oven at 250 °C in the air. The hBN coated Cu foil showed a dramatically smaller oxidized area after 100 hours in the oven than bare Cu foil at the same conditions after 2 hours. The protective layer was commercially available CVD grown hBN film. However, the anti-corrosion of hBN film depends on its quality. The oxidation appeared mainly within areas where defects in hBN film were, as the study describes [54].

Hexagonal boron nitride creates atomic flat planes which are relatively free of dangling bonds and charge traps [55]. Additionally, hexagonal boron nitride is an insulator with a direct wide band gap. Thus hBN is an ideal dielectric substrate for electronics based on 2D materials such as graphene. The report utilizing density functional calculations presents a band gap opening in graphene placed on hBN. The study focused on the mono-layered graphene in specific relative positions to hBN [51]. Such a fact would be more than suitable for a wide range of GFETs applications.

In addition to the previously mentioned applications, hBN could be also applied in optics as a substrates, or gate dielectrics for 2D electro-devices, as a gas detector, in batteries, or a wide range of nanocomposites. Hexagonal boron nitride could be also functionalized or doped in a similar way as graphene altering its properties [56].

1.2.3 Other 2D Materials

Two-dimensional materials are characterized by two macroscopic dimensions in two axes and one nanoscopic in the third axis. The thickness of such a material is usually in the order of nanometers sometimes even in atomic. Properties of 2D materials differ significantly from their three-dimensional forms. The enthusiasm in 2D materials started with graphene and it still ranks among the 2D materials which receive the most attention of the research community and even of many commercial companies.

Many elements and compounds were experimentally observed or are predicted to posses 2D form like metals, chalcogens and other groups through-out the whole periodic table (graphene, 2D platinum, stanene), their combinations (MXenes, 2D oxides, and hydroxides), minerals, alloys and clays (kaolinite) or different forms of the known 2D material - 2D supracrystals (T-graphene) and the list goes on.

Silicene and Germanene

Silicene and germanene are materials with honeycomb crystal structure and sp^2 orbital hybridization similar to graphene made of silicon and germanium respectively. The calculations indicate that free-standing silicene may exists and honeycomb structure could posses two forms. The first one is just mentioned silicene and the second is Si(111) with atoms bonded via sp^3 hybridization. This bond is responsible for vertical displacement of silicon atoms in Si(111). Both 2D materials are expected to be semiconductors with zero band-gap or metals and exhibit Dirac cone with mass-less electrons similar to graphene [57]. Electron dispersion relation of graphene is further discussed in section 1.10.

The silicon atoms prefer bonding via sp^3 rather than sp^2, thus causing the preparation of its 2D allotropes to be more difficult. One of the very first experimental proofs of silicene existence came in 2010. The silicene was grown epitaxially on a tight-packed surface of Ag(111) at elevated temperatures. 2D silicone structure was prepared under ultra-high vacuum (UHV) and the precious rate of Si deposition. Still, silicene prepared in such a way was not perfectly flat, indicating possible sp^2-sp^3 hybridizations with Si(111).

Germanene could be grown in a similar way as silicene for example on the surface of Pt(111) with deposition under UHV. The formed 2D layer buckled hexagonal structure related to interaction with the platinum substrate. The formation of the honeycomb structure was also calculated to be the most stable configuration for the germanene/Pt(111) system [58]. Other theoretical studies suggest the application of buckled silicene and germanene in FETs with higher on/off ration which is not so well managed in graphene-based FETs. The simulation also suggested a possibility of the band gap formation when the external electric field applied in a favor of Si and Ge 2D allotropes in contrast to planar graphene [59].

The motivation behind the research of these materials is the fact that silicon and germanium are crucial elements of today's semiconductor industry. This industry has well-established procedures thus offering the potential to easier use these 2D materials in many other applications.

Molybdenum Disulfide

MoS_2 can be naturally found inorganic solid compound containing a covalently bonded layer of molybdenum sandwiched between two layers of sulfur. MoS_2 also shows hexagonal crystal superstructure. Van der Waals weak interaction holds individual layers of MoS_2 together and makes it easy for layers to slip over each other. This is why is MoS_2 extensively used as a tribomaterial and dry lubricant. MoS_2 also displays a direct band gap of circa 1.8 eV. Molybdenum Disulfide found its applications as a catalyst during hydrogen evolution, hydrogen storage, elastic materials, coating materials, or in Li-ion batteries [60].

The interesting about MoS_2 and other 2D materials could be also their combinations to achieve new properties and characteristics of so-made devices or composites. One of the examples might be multilayered heterostructure for electronics made of different 2D materials. FET was constructed of CVD grown bi-layered graphene as a source and drain to contact a few-layer MoS2 flake, exfoliated hBN as a top-gate dielectric and exfoliated graphene as a top-gate electrode. This microdevice showed small electron mobility with n-type characteristic and high on/off current ratio of around 10^6. The FET exhibited stability of mobility value at high gate fields superior to conventional silicon-based FETs. The same study also presents another similar WSe_2-based device with p-type electronic characteristics showing the versatility of 2D materials electronics with only van der Waals interactions [61].

1.3 Preparation of 2D materials

One of the major drawbacks of wider applications of graphene is the lack of fabrication methods which would not only provide high quality graphene but also could be scaled up for industrial needs. The application of graphene by many industries holds back the vacancy of graphene large scale production despite its excellent properties.

Many different methods have been explored and proved as valuable approaches to produce graphene or other 2D materials in immense areas of industry. Some methods like *epitaxy* are well-established in semiconductors production or relatively new like *flash synthesis* of graphene for which an unusual source of carbon could be used like discarded food, rubber tires or mixed plastic waste. Three important and well-known methods of 2D materials preparation will be discussed in further paragraphs.

1.3.1 Chemical Vapor Deposition

The principle of chemical vapor deposition (CVD) growth is the introduction of gaseous 2D material feedstock onto the surface of metal under high temperatures. The metal surface plays a crucial role during the CVD process as a catalyst for a feedstock molecule decomposition and subsequent thin-film growth. Chemical vapor deposition method has been used for the growth of thin films for many years, one of the first reports of CVD grown graphene is from 2009. In this study, methane was used as a precursor for graphene growth on a copper foil. The methane molecule underwent reaction on metal surface which led to graphene growth. Copper is essential for methane decomposition making this process self-limiting and easier to control. All has been done under H_2 atmosphere to help copper etching and thus enhanced the quality of the product [62]. Another study prepared graphene on nickel [63], in which carbon atoms dissolved at a certain temperature and precipitated into the surface during cooldown to form graphene on the top of the surface. Many other metals, liquid metals, oxide compounds, various glasses, and flexible materials were adapted as graphene CVD grow substrates [64] yet nickel and copper remain the most popular and the most explored.

Quality of CVD grown graphene does not reach the quality of exfoliated graphene. The main flaw of this method is the necessity to transfer the graphene to a non-conductive substrate thus exposing graphene to impurities and inducing undesirable additional defects [64]. Despite these shortcomings, some recent studies presented CVD graphene in quality rivaling its exfoliated counterpart. For example, L. Banszerus *et al* [65] reported ultra-high quality graphene prepared by CVD technique using CH_4 as a precursor and Cu foil copper as a growth substrate. The key step of the study was the advanced transfer process based on van der Waals forces minimizing contamination of the graphene. Their device made of graphene encapsulated between two hBN layers exhibited charge carrier mobility over $300\,000\,\mathrm{cm^2V^{-1}s^{-1}}$ at low temperatures [65]. On the other hand, the CVD method could be scaled up. The size of grown thin films is only limited by dimensions of a used substrate and CVD reactor. The large scale samples could by prepared by CVD, for example with the specialized design of the CVD reactor a 100 m long high-quality graphene sample was prepared employing roll-to-roll CVD synthesis on a suspended copper [66].

1.3.2 Epitaxial Growth

Epitaxy is a process during which a thin crystalline layer grows on the surface of a single-crystal substrate. The crystalline lattice of the newly formed layer takes over the crystalline structure of the substrate. This is called parallel epitaxial orientation but it is not always the case, in general. The epitaxial orientation depends on the temperature. Growth also induces stress to the newly formed layer because the substrate and epitaxial layer both differ energetically (chemical bonds) and geometrically (lattice mismatch). No structural mismatch may be present during homoepitaxy during which is for new layer and substrate used the same material. If there is no difference in energetic and geometric aspects of the system, the materials are identical, the growth could be labeled as crystal growth or autoepitaxy. Heteroepitaxy is a kind of epitaxy where materials of newly formed film and substrate are different. The new epitaxial film will have a single orientation relative to the substrate [67].

The process of epitaxy is very well adapted in the semiconductor industry. It is de facto the only affordable method for the high-quality growth of numerous semiconductor materials and a diverse number of semiconductor-based devices. Nevertheless, semiconductors are not the only material produced by epitaxial growth. Wafer-scale single-crystal hBN epitaxial growth on Cu(111) thin film has been just reported [68]. Although the hBN growth on Cu(111) is widely believed to be impossible, one study presented hBN monolayer grown on a Cu(111) thin film across a two-inch sapphire wafer. Executing polymer-assisted electrochemical transfer the quality of so grown single-crystal hBN has been demonstrated on the enhancement of mobility in MoS_2-based device.

Epitaxy could also be used for further more complex structures as performed in [69]. Researchers managed to epitaxially grow large-area single-domain graphene on hBN by a plasma-assisted deposition method. Again, the scale of grown materials was only limited by the size of the hBN substrate. The process might be applicable to other flat surfaces as researchers suggest. This implies that epitaxy might also have the capability to produce graphene and other 2D materials in an extensive amount, quality, and controlled manner.

Effect on Graphene

1.3.3 Micromechanical cleavage

Micromechanical cleavage (MC) also known as the Scotch tape method or a micromechanical exfoliation is one of the oldest methods for thin film preparation and has been used for decades, e.g. in crystallography. The study that started graphene phenomenon used exfoliated few- and mono-layers of free-standing graphene of a lateral size of a few µm [23]. This study analyzed electrical properties of so prepared flakes and later led to the "Graphene revolution" in 2D materials. This method is still one of the most popular among graphene-related research community due to its simplicity and high quality of produced thin materials.

No cutting-edge technology is needed for MC, only adhesive tape is required. The source for a graphene is graphite flake pieces which is placed between the adhesive tape. When peeled off cleaved thin flakes of graphite adhere to the surface

of the tape and may have an atomic flat surface thanks to weak van der Waals bonding between the graphene layers within graphite. To get thin few-layered graphite a new clean piece of tape is applied to cleavage before peeled-off flake. In other words, simple repetition of cleavage with clean adhesive tape breaks graphite flake into thinner and thinner pieces until the mono-layered graphene is achieved.

Many other methods based on the breaking van der Waals interaction between the layers of graphite exist. *Liquid-phase exfoliation* is based on exfoliating in liquid media via ultrasound or shear forces to extract mono- to few-layer material sheets [70]. Graphene could be produced via the *reduction of graphene oxide*, where oxidants intercalate graphite and introduce functional oxygen groups on the surface of graphene layers know as the Hummers' method [71]. This technique is low-cost, has a high scalability potential, and excellent yield yet utilizes potentially dangerous chemicals. Another simple, low-cost, and effective method for 2D material production is the *mechanical milling* utilizing e.g. a planetary mill and a solvent. Milling has the potential for large scale production but it also induced defects in the final products [72]. a well-known technique of *electrochemical exfoliation* may produce graphene as well. The method commonly used for aluminum production could be adjusted for example for natural graphite exfoliation [73]. Electrochemical exfoliation is an environmentally friendly method with the possibility of mass production of graphene at a much lower cost but more improvements must be made.

The MC produces one of the highest quality 2D materials. Many of the before mentioned sensational properties of graphene (chapter 1.2.1) have been measured on exfoliated samples. The exfoliation is a simple and versatile technique for not only defect-free graphene, but also many other 2D materials, e.g. MoS_2, WeS_2, or hBN. Compared to other methods, exfoliation produces relatively small size flakes. However, with proper adjustments, it may produce flakes with ca. centimeter in size [74]. Despite the benefits of the exfoliation, the scalability of this method is its main drawback and MC remains as the preeminent technique for fundamental research and exploration of graphene properties and potential applications.

More details about the exfoliation method will be presented in the *Experimental part* of this thesis.

1.4 Effect of Substrate on Graphene

The substrate has a crucial role in affecting the quality of graphene during its the growth as well as in a final setup for analysis or applications of graphene. For example, during the CVD method the surface imperfections, grain boundaries, and impurities of the metal surface can cause graphene defects. The CVD substrate is usually annealed at high, nearly melting temperatures under a hydrogen atmosphere to remove adsorbed impurities and to mitigate other negative effects. a monocrystalline atomic flat substrate is suitable for CVD or epitaxial growth of 2D materials. It is also important to have fine-tuned factors of the growing process like temperature, pressure, grow time, or substrate material for a high-quality output of procedure.

Commonly used substrates for graphene analysis is SiO_2/Si. It is an available and well-established substrate. The utilization of this substrate has one advantage, which is a simple identification of graphene thin layers thanks to the easily perceivable optical contrast in an optical microscope as can be seen in Fig. 1.9 in the chapter 1.2.1. Unfortunately, the SiO_2 substrate layer also has some limiting effects on some graphene properties. Charge carrier mobility has been studied both theoretically and experimentally. Mobility of mono-layered graphene seems to be primarily limited by the SiO_2 substrate as data and models suggest [75].

There have already been studies focusing on different substrate material like SiO_2, other semiconductor, and metals. Nevertheless, the graphene on a top of many substrates is very uneven and has wrinkles, which could suppress graphene properties as experiments have shown. In a past few years a lot of articles have proved hBN as a superior substrate to SiO_2 and other graphene substrates. As mentioned in the chapter 1.2.2 hBN has similar crystal structure, insignificant lattice mismatch, and it can be produces with very smooth surface which lacks charge traps and it electric insulator. Many of the hBN properties make it well-sufficient substrate for graphene and its electronic applications [76].

For a simple comparison, devices both made of exfoliated graphene with minimum impurities but with SiO_2/Si or hBN as a substrate have shown substantial difference in the values of charge carrier mobility. The highest values of mobilities for SiO_2 based devices (not suspended graphene) are usually in tens of thousands of $cm^2V^{-1}s^{-1}$. On the other side, the devices which used hBN as substrate reports mobilities more then 10 times higher [77]. Thus implying hBN as one of the best substrates for graphene and its applications.

1.5 Atomic Force Microscopy

The idea behind the atomic force microscopy (AFM) is to measure the forces between the sample surface and the scanning tip of the probe to track the surface topography of the sample. To simply present interaction between the tip and samples surface a Lennard-Jones potential V_{LJ} is used as a model potential:

$$V_{LJ} = \epsilon \left[\left(\frac{r_{\mathrm{m}}}{r} \right)^{12} - \left(\frac{r_{\mathrm{m}}}{r} \right)^{6} \right],$$

where ϵ is the lowest value of potential, the bottom of the potential well, r_{m} is the distance at which the potential equals its minimum and r is the distance between the particles. This potential has its repulsive ($\propto 1/r^{12}$) and attractive ($\propto -1/r^{6}$) part. Lennard-Jones potential summarizes the long-range attractive van der Waals force and the short-range forces, such as chemical bonding forces and others contributing to the tip-sample interaction.

The AFM probe consists of the cantilever with the finely sharpened tip, which end is ideally occupied by only one atom. The effect of the analyzed surface on the tip of cantilever can be detected with a laser. The laser beam is reflected on the cantilever onto the photodetector. The position change of cantilever induces deflection of the beam from which a surface topography could be determined as depicted in Fig. 1.11. Besides the beam deflection method, several other methods can be used to detect the motion of the AFM cantilever like interferometry, piezoresistance, or piezoelectric detectors.

AFM may work in three basic modes. The first is *constant force* (contact mode) during which a certain force setpoint is kept constant by feedback during scanning of the surface. In the second is *constant height* (non-contact) mode is cantilever held at constant height above the scanned surface. During the third mode, the *tapping mode* is the cantilever oscillating at a fixed frequency and amplitude. The shape of the surface is detected via the frequency shift of oscillation.

AFM samples do not require any special treatment. The AFM provides a three-dimensional real-space surface profile and works properly in ambient air or a liquid environment. AFM can provide atomic resolution in UHV and can be combined with other techniques too. The disadvantage of AFM is possible artifacts and deformations in the final image induced by imperfect scanning tip, its damage, adhered particles, or even by its shape. The AFM has relatively slow scanning speed and a small scanning window because the precise movement of the cantilever is provided by the piezo crystals. E.g. in contrast to the scanning electron microscopy (SEM) which is able to scan large areas in real-time [78]. Yet, AFM offers many advantages and remains a significant tool in nanoscience.

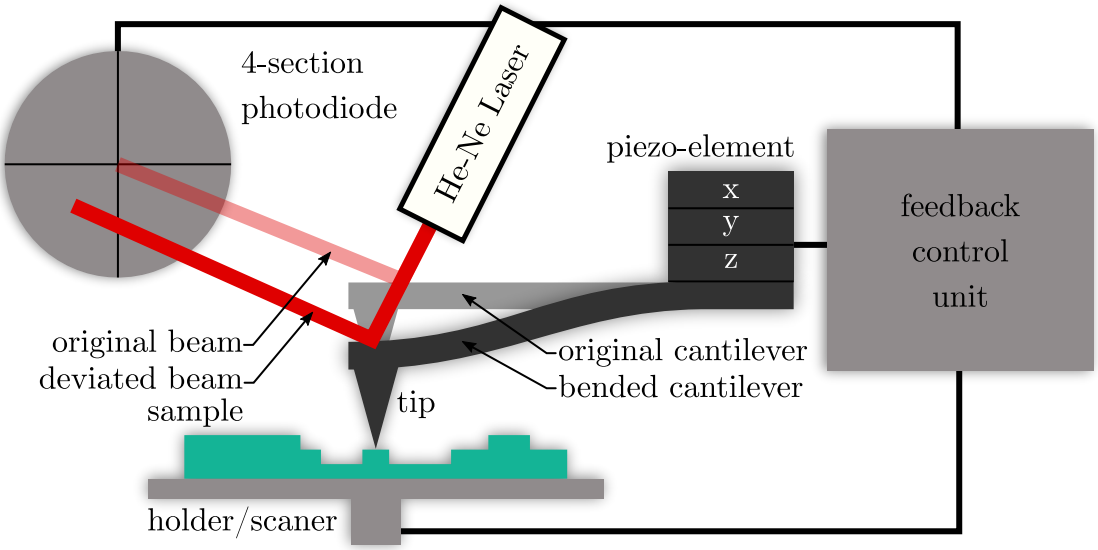

Fig. 1.11: The AFM provides a three-dimensional real-space surface profiling. The interaction between the cantilever tip and the surface could be observed through the laser beam deflection. AFM may provides atomic resolution but the final image quality is affected by the quality of scanning tip and scanning mode.

1.6 Raman Spectroscopy

Raman spectroscopy is a powerful, non-destructive spectroscopic method for characterizing the lattice structure, its electronic, optical, and phonon properties of a diverse variety of materials with high resolution. Almost a century ago, C.V. Raman published his work on light scattering in materials, today known as Raman scattering. The method is based on inelastic scattering of light in material which results in a difference between the energy of incident and scattered photons, representing the characteristic of the material - the Raman fingerprint of a material. The incident light can lose its energy to fundamental excitations in the system (Fig. 1.12 a)), typically phonons, or can gain energy from the same excitations. These processes (Fig. 1.12 b)) lead to Stokes and anti-Stokes Raman spectral peaks, respectively (Fig. 1.12 c)). The Raman scattering obeys the conservation of energy and momentum [79].

Raman spectroscopy is a very helpful method for identifying graphene, its quality, and its thickness. Few-layered graphene exhibits a characteristic Raman features in spectra depending on the number of layers and their mutual orientation. Most frequently, these graphene measurements are done on the SiO_2/Si substrate at room temperature. Such a spectrum of high-quality graphene has a characteristic shape with two significant peaks: the G peak around 1600 cm^{-1} and $2D$ peak at 2700 cm^{-1}. The low-quality graphene may be identified by the D peak around 1350 cm^{-1} which indicates defects in the crystal and is the most significant broad peak for the amorphous carbon. With the ascending number number of layers, changes in the shape and position of peaks can be observed. The $2D$ peak of graphite has a noticeable shoulder implying an interaction between the individual layers. The G peak also

gains intensity with the number of layers [80], which offers the ability to distinguish mono-, bi- or few-layered graphene with Raman spectroscopy.

The number of few-layered hBN could be also determined by Raman spectroscopy. Hexagonal boron nitride has two characteristic peaks as well. The in-plane mode around 1370 cm^{-1} and interlayer shear mode around 50 cm^{-1}. The position of the low-frequency peak is defined by the number of hBN layers. The in-plane mode is not much affected by the number of layers, yet it exhibits a more apparent temperature dependent peak shift [81].

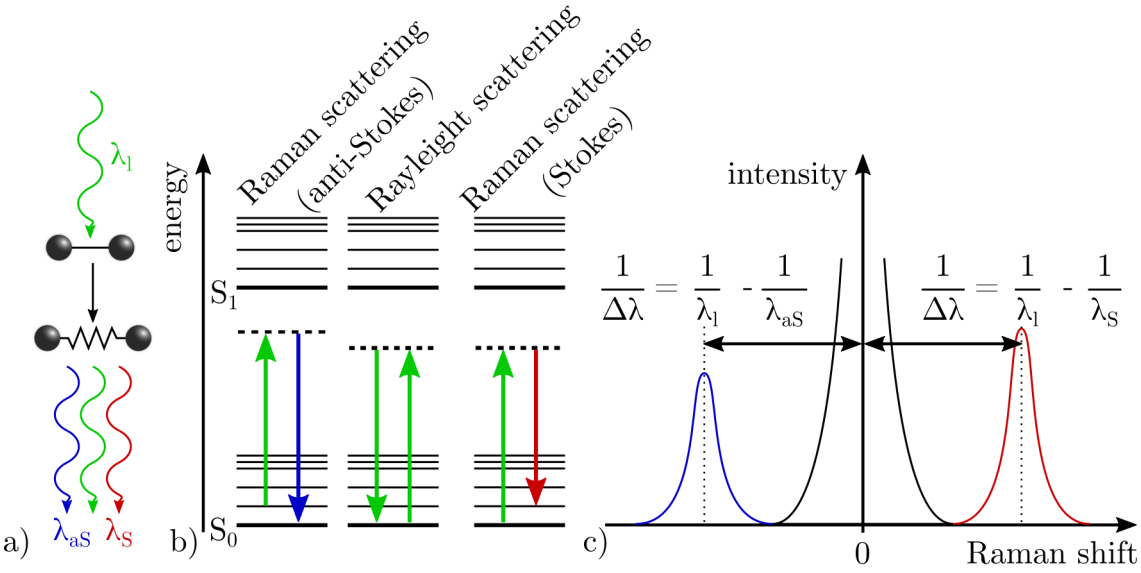

Fig. 1.12: Raman spectroscopy is based upon the interaction of the electromagnetic ray with the crystalline structure of the measured material. a) the interaction of the initial ray λ_I with the observed molecule leads to the excitation of the molecule. The molecule then deexcites in one of the three ways. By emission of the anti-Stoke ray λ_{aS} with a shorter wavelength and higher energy, the ray with the same wavelength and energy, or the Stokes ray λ_S with a longer wavelength and lower energy. b) these rays originate from the three different energy transitions within the molecule. The energy of the emission rays depends on the difference between the excited (dashed line) and the final energy state. The final state can have higher, same, or lower energy than the initial energy state. c) the intensity and the Raman shift compare to the initial reciprocal wavelength of the emission rays is depicted at the diagram with the corresponding equations of the Raman shift of detected rays. Color of the rays and the peaks correspond to the blue or red wavelength shift. The position and intensity of the peaks are related to the initial ray wavelength and properties of the measured materials. Each material also has its own Raman fingerprint - specific spectrum.

1.7 Electron-beam lithography

Electron-beam lithography (EBL) is a method for fabricating nanoscale features with a focused electron beam in electron-sensitive film. Such films are called *resists* and their certain chemical properties change after exposure to electron irradiation. The e-beam patterning is computer-controlled trough the stage position or with a focusing system of scanning electron microscope (SEM). An EBL instrument is in one way a SEM used for writing instead of reading thus as SEM it consists of three essential parts: an electron gun, a vacuum system, and a control system. An electron gun generates, accelerates, focuses, and projects an electron beam onto the sample. For proper focusing and overall gun performance a vacuum system is needed, pressure in the gun system is around $1 \cdot 10^{-8}$ Pa, and circa $1 \cdot 10^{-6}$ Pa in a sample chamber.

Various chemical reactions take place inside the resist material due to electrons scattering. Such an interaction alters properties of resist at the exposed areas to the electron beam, usually changing resist solubility. This local modification of resist enables selective removal of resist in a solvent, this step is called the *resist developing*. Selective removal of resist creates a pattern in the film. The pattern may serve as a template for additional material deposition e.g. during metal evaporation, thus supporting the creation of structure. The removal of excessive deposited material and the rest of the resist (while the desired patterned structure remains on the substrate) is called the *lift-off* process.

There is a wide variety of resists that differ by the used substrate, additional chemicals, depositions method, or dimensions of the patterns. a resist is usually a polymeric solution applied onto the substrate by the *spin coating* method and dried by baking to a homogeneous thin film. These materials are divide into two main categories - positive and negative resists. The exposed part of the *positive resist* is removed during developing, or remains in the case of the *negative resist* it remains on the sample. The versatile standard of resists is the poly(methyl methacrylate) (PMMA) family of resists [82]. The lithography process with positive resists and additional information is described in the *experimental* part of the thesis.

1.8 Electron Beam Evaporation

The very base principle of electron beam evaporation (EBL) is transferring the energy of the focused electron beam to the evaporant – deposition material causing it to evaporate so it may condense upon a substrate. E-beam evaporation instruments have three main parts: the electron gun, the beam deflection lenses, and the crucibles - containers of deposition material. The electron emission takes place on the heated tungsten filament. The electron beam is formed in the gun which is usually placed underneath or next to the crucibles holder to avoid unwanted filament contamination. High voltage is applied to accelerate the beam. The magnetic lenses focus electron beam onto the crucible trough the 270- or 180-degree rotation. Interaction of electrons and the surface of material causes it to sublimate and covers everything in the chamber within the line of sight. Overheating of crucibles could be regulated by water cooling [83].

The chamber must be under a high vacuum (pressure $<10^{-8}$) to ensure the mean free path to be long enough for the evaporated particles to reach the substrate. The deposition rate and thickness of the deposited film are generally measured with quartz crystal microbalance (QCM) implanted in the deposition chamber. The QCM is measuring mass variation per unit area through a change of frequency of a quartz crystal resonator. The schema of the electron beam deposition apparatus is depicted in Fig. 1.13.

Electron beam evaporation is capable of deposit materials with high sublimation temperatures like tungsten or graphite at a high deposition rate compare to thermally induced evaporation. The proper focus of the electron beam provides the deposition of films with high purity without any contamination from other neighboring crucibles. The e-beam evaporation equipment is usually complemented with motorized carousel and multiple materials enabling the deposition of heterogeneous films during one session thus being a useful method for nanofabrication.

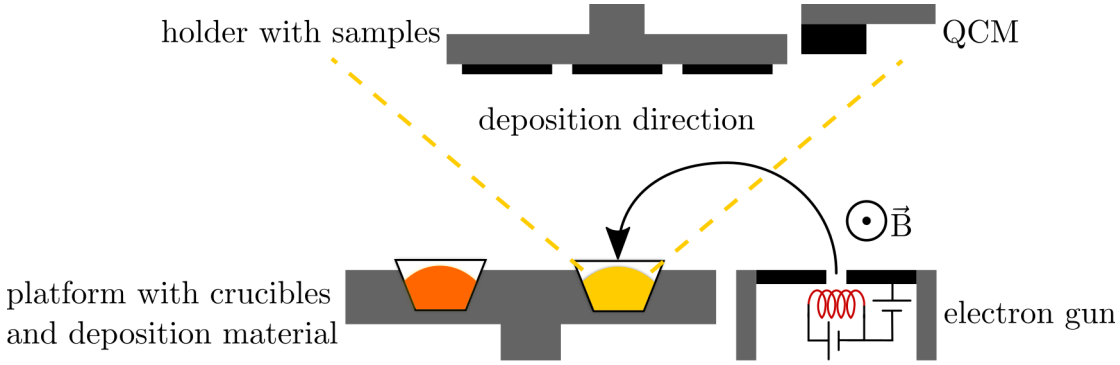

Fig. 1.13: E-beam bent by magnetic field $\vec{B}$ and focused by electron gun heats up material only in one crucible. So evaporated particles sublimate on everything within the line of sights. Deposition rate is measured with quartz crystal microbalance.

1.9 Low-Energy Electron Microscopy

Low-energy electron microscopy (LEEM) is a surface-sensitive analytical method. LEEM setup has many similar parts to typical transmission electron microscope yet a few differences play an important role. The analyzed specimen is illuminated from the objective side because it is not transparent for slow electrons and such an illumination creates the need for a separation between the incident and reflected beam. The simplified construction of the LEEM instrument shows Fig. 1.14.

The source of electrons is usually field electron gun. Electrons are accelerated at the energies of $15 - 20\,\mathrm{keV}$. These "fast" electrons are then decelerated in front of the specimen to the desired low energy of (0-50)eV. The deceleration could be provided by the cathode objective lens or by the additional potential applied the specimen. Slow electrons afterwards interact with the surface of the specimen. The interaction includes elastic, inelastic scattering, phonon excitation, or diffraction. The back-scattered electrons are re-accelerated, deflected by electron separator into the condenser optics, and detected on the imaging plate – a phosphorescent screen or a CCD camera. The image contrast is caused by differences in selectivity of individual parts of the specimen like differences in crystal orientation, surface reconstruction, adsorbates on a surface, different azimuthal orientations, or topological disparities [84].

LEEM technique has diverse variants to obtain numerous surface characteristics. *Low energy electron diffraction* (LEED) method focuses on periodicity of surfaces illuminated by a parallel beam of electrons through the diffraction patterns. The topography image and phase-contrast might be seen in a *bright field* mode. The *dark field* mode shows a contrast of different phases based on selected area spots. Different structures of a surface may be identified by LEEM *spectroscopy*, which could be also used for a thickness determination of 2D materials like graphene, hBN, or MOS_2. *Photoemission electron microscopy* (PEEM) imagines secondary electrons excited with photons of different polarization and wavelengths. LEEM is an overall helpful technique for surface analyses and able to gather various information about a surface as its structure, topography, or magnetic and chemical properties [85].

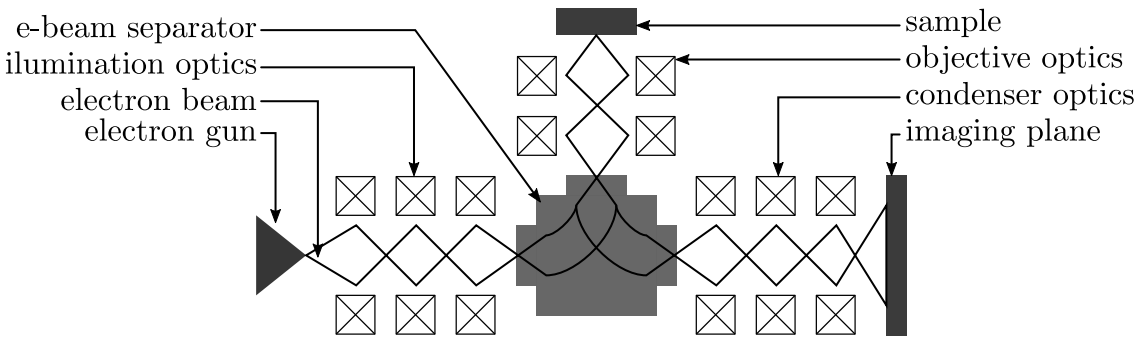

Fig. 1.14: Schematic illustration of low-energy electron microscope. The analyzed specimen is illuminated from the objective side. After the interaction with a sample, the back-scattered electrons are re-accelerate back and deflect by electron separator into the condenser optics, and detected on the imaging plate.

1.10 Charge Carrier Mobility

Many phenomenal properties of graphene are related to its quality which could be characterized by charge carrier mobility as will be shown in this chapter.

An electron with charge e placed in the electric field $\vec{E}$ experiences a force equal to $\vec{F}_E = -e\vec{E}$ called electric force which has the opposite direction to the electric field. An electron with zero initial velocity then has a straight-line trajectory. An electron with a non-zero initial velocity has trajectory given by the mutual orientation of the electric field and the direction of the initial motion of the electron.

An electron moving in a plane perpendicular to the magnetic field $\vec{B}$ shall experience the magnetic force $\vec{F}_M = -e(\vec{v} \times \vec{B})$ as well, with $\vec{v}$ – electron velocity vector. The effect of the magnetic field will be manifested in the circular motion of the charged particle. The radius of such a motion is $r = m_e v/Be$ caused by the centripetal force $F_C = m_e v^2/r$, which affect electron with constant velocity v and the mass m_e.

Electron kinetic energy remains constant only the velocity vector changes, the magnetic field does no work.

The Lorentz force $\vec{F}_L$ is the result of an electromagnetic field affecting a moving charged particle. For example, an electric field acts in the x-axis direction and a magnetic field in the z-axis direction. An electron moving along the xy-plane will be affected via $\vec{F}_L = -e(\vec{E} + \vec{v} \times \vec{B})$. The equations of motion will be:

$$m_e \frac{dv_y}{dt} = -ev_x B_z \text{ and } m_e \frac{dv_x}{dt} = -e(E_x + v_y B_z). \tag{1.1}$$

the equations for each velocity will be then:

$$v_x = -(v_{0y} + v_D)\sin(w_C t) + v_{0x}\cos(w_C t), \tag{1.2}$$

$$v_y = -v_D + v_{0x}\sin(w_C t) + (v_{0y} + v_D)\cos(w_C t). \tag{1.3}$$

the trajectory of electron is described by coordinates as:

$$x = \int v_x dt = \frac{(v_{0y} + v_D)}{w_C}\cos(w_C t) + \frac{v_{0x}}{w_C}\sin(w_C t) + x_0, \tag{1.4}$$

$$y = \int v_y dt = -v_D t - \frac{v_{0x}}{w_C}\cos(w_C t) + \frac{(v_{0y} + v_D)}{w_C}\sin(w_C t) + y_0. \tag{1.5}$$

The constants x_0 and y_0 are initial coordinates, v_{0x} and v_{0y} are initial velocities of electron in x and y-axis respectively. The variable $w_C = eB_z/m_e$ is the cyclotron frequency and $v_D = E_x/B_z$ is the drift velocity. Just described equations are summarizing the movement of a charged particle in the electromagnetic field. The movement of such a particle is the cycloid along a circle with angular frequency w_C, the center of the circle is also constantly moving in y-axis with the drift velocity v_D. The electrons may perform this movement in ideal 2D film at any non-zero magnetic field.

The movement of electrons differs in a finite film with defects or and weak magnetic field, there may be a situation when an electron is not able to complete the cycle. The time between the collisions τ is small or the magnetic field is weak, thus $eB_z/m_e\tau < 2\pi$. The electron moves in a random direction after the scattering in a similar way as without defects until it is scattered again. The electron will move at a drift velocity, but not only in the direction of the y-axis. Further calculations assume random direction of electron movement after a collision, such a change in direction is instant. The drift velocity maybe then expressed as:

$$V_{Dx} = -v_D \frac{w_C\tau}{1 + w_C^2\tau^2}, \tag{1.6}$$

$$V_{Dy} = -w_C\tau v_D \frac{w_C\tau}{1 + w_C^2\tau^2}. \tag{1.7}$$

If the time between the scattering events is large ($\tau \to \infty$) and then $v_{Dx} \to 0$ and $v_{Dy} \to -v_D$ as in the situations without the scattering. The zero magnetic field implies $v_{Dy} \to 0$ and $v_{Dx} \to -E_x e\tau/m_e$ which is situation with the particle affected only by an electric field. The constant of proportionality between drift velocity and electric field at zero magnetic field is called *charge carrier mobility*:

$$\mu = \frac{e\tau}{m_e}. \tag{1.8}$$

The current density vector $\vec{J}$ describes the electric current per cross-sectional area in the direction given by the motion of the charges and could be expressed as $\vec{J} = \rho\vec{v}$, where ρ is charge density and $\vec{v}$ is the charge velocity. For the 2D situation, it is $\vec{J} = -n_e e\vec{v}_D$, where the n_e is charge areal concentration, e.g. The number of electrons per square meter. The components of $\vec{J}$ are

$$J_x = -n_e e\vec{v}_D x = \frac{n_e e^2\tau}{m_e} \frac{1}{1 + w_C^2\tau^2} E_x, \tag{1.9}$$

$$J_y = -n_e e\vec{v}_D y = w_C\tau \frac{n_e e^2\tau}{m_e} \frac{1}{1 + w_C^2\tau^2} E_x. \tag{1.10}$$

The vector form of Ohm's law $\vec{J} = \hat{\sigma}\vec{E}$ describer linear relation between the current density and the electric field. The proportionality constant of this relation is specific conductivity tensor $\hat{\sigma}$

$$\hat{\sigma} = \begin{pmatrix} \sigma_{xx} & \sigma_{yx} \\ \sigma_{xy} & \sigma_{yy} \end{pmatrix} = \begin{pmatrix} \sigma_{xx} & -\sigma_{xy} \\ \sigma_{xy} & \sigma_{xx} \end{pmatrix} , \tag{1.11}$$

where $\sigma_{xx} = \sigma_{yy}$, $\sigma_{yx} = -\sigma_{xy}$ and

$$\sigma_{xx} = \frac{n_e e^2 \tau}{m_e} \frac{1}{1 + w_C^2 \tau^2}, \tag{1.12}$$

$$\sigma_{xy} = w_C \tau \frac{n_e e^2 \tau}{m_e} \frac{1}{1 + w_C^2 \tau^2}. \tag{1.13}$$

The specific electrical resistivity is defined as $\rho = RS/L\,[\Omega\mathrm{m}]$, where R is the electrical resistance of specimen, A is the cross-sectional area of the specimen and L its length. For the 2D examples such as graphene it the specific resistivity $\rho = RW/L\,[\Omega]$, where R and L are the same variables. Yet, W is the width of the specimen. The resistivity is also defined as the reciprocal of conductance. Thus in the case of the tensor $\hat{\sigma}$, resistivity can be described as:s

$$\hat{\rho} = \begin{pmatrix} \sigma_{xx} & -\sigma_{xy} \\ \sigma_{xy} & \sigma_{xx} \end{pmatrix}^{-1} = \begin{pmatrix} \rho_{xx} & \rho_{xy} \\ -\rho_{xy} & \rho_{xx} \end{pmatrix} , \tag{1.14}$$

where ρ_{xx} is longitudinal and ρ_{xy} is transverse element of resistivity tensor which are

$$\rho_{xx} = \frac{\sigma_{xx}}{\sigma_{xx}^2 + \sigma_{xy}^2} = \frac{m_e}{n_e e \tau}, \tag{1.15}$$

$$\rho_{xy} = \frac{\sigma_{xy}}{\sigma_{xx}^2 + \sigma_{xy}^2} = \frac{B_z}{n_e e}. \tag{1.16}$$

The element ρ_{xy} is independent of τ and element ρ_{xx} is independent of magnetic field B_Z. That is convenient for the charge mobility μ expression, because the combination of equations 1.8 and 1.15 results in

$$\mu = \frac{1}{n_e e \rho_{xx}}. \tag{1.17}$$

Equation 1.17 is often called the Drude model of electrical conduction. The Drude treats electrons as particles of classical ideal gas. Electrons are bouncing off much heavier immobile positive ions like in a pinball machine.

The charge carrier mobility is strongly affected by defects and imperfection of 2D layers. As mentioned in chapter 1.2.1, the conduction of graphene is linearly symmetric near the Dirac point. The mobility of holes and electrons should be equal. Reported mobilities span a wide range from 20-200000 $\mathrm{cm^2V^{-1}s^{-1}}$ with a long mean-free path of in a range of µm. The mobility has weak temperature dependence which indicates that impurities and defects are the dominant limitation factors [35].

One of the most common ways to measure graphene charge carrier mobility is at the field-effect transistor. Such a setup will be discussed more in details in the *experimental* part of this work as well as procedures of preparation, identification of graphene and hBN.

2 Experimental part

The following part of this work describes each of every step taken from 2D material preparation to final measurement at the field-effect transistor setup. Thin films were prepared with micromechanical exfoliation method. Later analyzed with methods like Raman spectroscopy or AFM. To create van der Waals heterostructure prepared for measurements preparation methods as EBL and e-beam evaporation were used.

The goal of the *Experimental part* is to prepare and to characterize heterostructure made of graphene and hBN. The quality of exfoliated graphene on hBN flake by the charge carrier mobility measurement. To create such a heterostructure an hBN and graphene were exfoliated using the Scotch tape technique with the addition of PDMS film and use of micromanipulator for precious graphene emplacement onto the hBN flake. Conductive paths had to be made to measure the electrical properties of graphene/hBN heterostructure. To obtain them multi-step lithography was utilized consisting of a spin-coating, thermal vacuum deposition, and lift-off process. Graphene layer can be damaged during any step of preparation so it was necessary to continuously monitor its quality. Raman spectroscopy has become the main tool for graphene quality analysis for its fast and precious execution. The AFM was used to fully characterize a topography of heterostructure, a thickness of hBN flake, and overall sample contamination. Conductivity measurement itself was carried on in graphene field-effect transistor setup using a specialized sample holder called the expander. Obtained data were processed according to the Drude model as one of the later sections describes. The following paragraphs are devoted to the mentioned steps in detail.

2.1 Graphene Exfoliation

Exfoliation plays a crucial role because the overall quality of the final device and the following operations depends on the aspects of exfoliated graphene and hBN flakes. Larger and undamaged flake is easier to work with compare to small uneven one.

The source of graphene for the exfoliation procedure was *Graphenium Flakes* from *NGS Naturgraphit*. These graphite pieces have circa 2 g each and 5–10 mm in size. The graphite piece was placed on the *Nitto* adhesive blue tape, then folded with the piece in between and slowly and gently peeled-off (Fig. 2.3 d)). The slow unfolding of tape leads to less transferred smaller pieces and flakes but of a higher quality compared to quick unfolding. If done correctly thinner pieces of graphite remain on the tape which could be seen with the naked eye. The goal was the largest and thinnest graphite (graphene being the best) flakes. To get thinner and thinner flakes just described step was repeated several times.

Unfortunately, every time the flake gets thinner it is also more vulnerable to deform or otherwise damage during the process. The best flakes were exfoliated after five folds of the tape but large and thin layers were also obtained even after ten folds. A new piece of the tape was used for each of the peel-offs. This guaranteed easier manipulation with flakes, easier peel-off, and better results.

The sheet of polydimethylsiloxane (PDMS) was cut into smaller pieces (5×5 mm) and placed on a cleaned microscope slide. The slide was cleaned using acetone and isopropyl alcohol (IPA). The slide cleaning minimizes the undulation of PDMS and thus providing higher quality transfer of flakes (Fig. 2.1 b) and (Fig. 2.3 e))). Dirty microscope glass may result in a wavy PDMS piece which then leads to complications during later graphene analysis, flake transfer, and the heterostructure assembly. The tape with thin flakes was placed on the top of the PDMS piece on the microscope slide. The tape was very gently pressed to ensure contact between flakes and PDMS. The glass slide was then placed on the hot plate for 5 min at 70 °C to enhance the adhesion between the graphene and the PDMS. After which the sample cooled down on the air. Other temperatures were tried as well. 95 °C and higher temperatures cause the tape to warp which leads to another unnecessary flake deformation. Temperatures under 50 °C had no visible enhance effect. After cooling, the tape is gently, yet swiftly peeled-off. The fast peel-off in this step ensures a greater number of flakes transferred onto the PDMS piece.

Mono-layered graphene flakes are practically undetectable by the human eye in a classical optical microscope. It is possible to distinguish thick graphite layers and thinner flakes but proper graphene detection has to be done. To evaluate the process of exfoliation one needs to use e.g. confocal microscope with Raman spectroscopy.

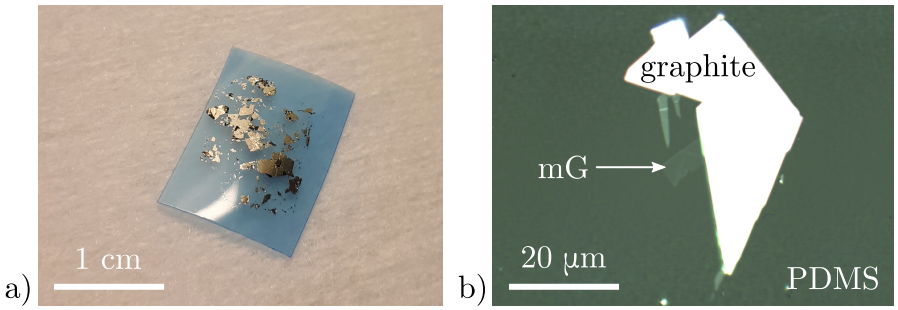

Fig. 2.1: a) Photo showing an example of the exfoliated graphite flakes on the adhesive blue tape. The flakes will be exfoliated several more times and transferred onto the PDMS piece for further, more detailed analysis. b) Graphite flake with mono-layered graphene (mG) and graphite flake on PDMS piece. Photo taken on optical microscope.

2.2 hBN Exfoliation

Hexagonal boron nitride is a suitable substrate for an electronics-based graphene application compare to silicone oxide [77] as described in section 1.4.

The exfoliation of hBN is done in a similar way as the graphene exfoliation. The source of flakes were hBN crystals purchased from *hq graphene*. The crystals are synthetic and have length circa 1 mm. hBN crystal was placed on the adhesive blue tape (Fig. 2.3 a)), then folded with the flake in between and quickly peeled-off just like during the graphene exfoliation. The peel-off step was generally done five to seven times (Fig. 2.3 b)).

Boron nitride flakes have to be placed on the silicon substrate (Fig. 2.3 c)). The used substrate was N-doped silicon with phosphorus and 285 nm thick layer of SiO_2 purchased from *ON Semiconductors Czech Republic*. Sample dimensions were 5×5 mm and 7×7 mm. Substrates had before pre-pared system of golden coordinates for the orientation on the sample, and golden pads for the graphene/hBN structure contacting. The SiO_2/Si substrates were acetone cleaned in ultrasonic bath for 5 minutes, which was repeated with the IPA, and than dried using N_2.

The piece of blue tape with hBN exfoliated flakes was placed on the cleaned substrate and placed on the hot plate for 5 minutes at 85 °C for better adhesion between the SiO_2/Si substrate surface and hBN flakes. The sample was then placed away after and the tape was quickly peeled off in order to get the maximum number of hBN flakes transferred onto the substrate. The aim of the hBN exfoliation is to get the largest flakes which may serve as a graphene substrate.

2.3 Flake analysis

The exfoliation result is the a large number of flakes, the graphene flakes on the PDMS and the hBN on the SiO_2/Si substrate. Flakes have to analyzed and the most suitable flakes marked for the following steps. This phase took place on the *Witec Alpha 300R* confocal Raman microscope. Samples (graphite and graphene flakes on PDMS) were analyzed using 532 nm laser wavelength, and power of 5-3 mW. The higher power of the laser was able to destroy the graphene films. Measurement usually had 15 accumulations at 0.5 s for each of them. The procedure started with an overall mapping of the whole PDMS piece followed by a more precious mapping and thinner flakes analysis. Suitable mono- and bi-layered graphene flakes were marked for the following step – the heterostructure creation.

In general, the analysis of hBN flakes did not need Raman spectra. Overall optical mapping of the whole SiO_2/Si substrate was done and then the positions of the best hBN flakes were marked. Flakes with the largest area and most even surface were chosen for the heterostructure assembly.

To summarized the graphene exfoliation, the bi- or the mono-layered graphene flakes were found on every second exfoliated sample. The dimensions of the graphene flakes were usually between few tens up to hundreds of square micrometers. The requirements for the hBN exfoliation were not so demanding. On every substrate at leas 3 suitable exfoliated hBN flakes were found. The examples of analyzed flake is in Fig. 2.2.

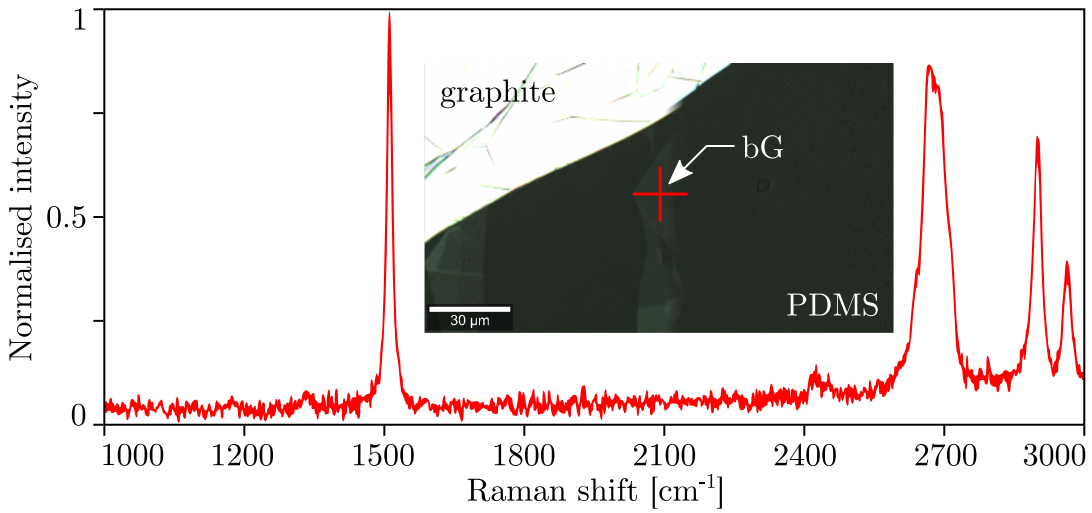

Fig. 2.2: Raman spectrum and photo of the graphene bi-layer - (bG) which was lately used for the heterostructure H21. Graphene was placed on the PDMS piece with many graphite flakes. Red cross marks the place of spectrum measurement.

2.4 Heterostructru Assembly

To place graphene on the hBN flake and thus create van der Waals heterostructure the microscope with the large working distance (WD) with hot plate and micromanipulator were used. The operation took place on the *4-probe station Cascade Microtech MPS 150* which offers a stage with a hot plate, vacuum nozzle for sample security, three objectives with 10X, 20X and 80X magnification, and metal rack available for additional devices. Setup was completed with a manual three-axial micromanipulator.

The hBN/SiO_2/Si samples were secured with a Kapton tape onto the stage of the microscope. The graphene/PDMS sample on the glass slide was attached to the micromanipulator using Kapton tape facing the stage (Fig. 2.3 f)). Glass slide was leveled and brought to the starting position a few millimeters above the substrate. Both flakes were preciously aligned over each other using the microscope optics and the micromanipulator (Fig. 2.3 g)). Proper alignment was also possible thanks to the transparency of the PDMS piece and the glass slide. The hot plate of the stage was afterward set to 85 °C to decrease adhesion between the graphene flake and PDMS.

Flakes were aligned in such a manner that a different focus of microscope optics showed either graphene flake or the hBN flake placed below it. By slow and cautious lowering the glass slide, the graphene flake was gradually approaching the hBN flake with additional corrections each step. Both flakes were visible just before the contact. The color of view field distinctly changed tone when was the PDMS piece in contact with SiO_2. Additional small glass slide lowering was performed to ensure complete contact of the PDMS piece and the substrate thus providing the best conditions for graphene to adhere to the hBN. Flakes stayed in contact for a minute after which a very slow and prudent retreat was performed. It was possible to repeat the full-contact phase if the graphene was not perfectly adhered to the hBN. But this correction would probably damage the thin films. It is also possible that the hBN flake stays on the PDMS piece. This was also possible to correct by repeating the full-contact step with no damage to graphene.

When performed correctly, graphene flake was easily visible on the hBN flake afterward (Fig. 2.3 h)). Whole process from exfoliation to the final assembly is in Fig. 2.3. Heterostructures were re-checked and photographed on *Witec Alpha 300R* again in detail for the following lithography process which demands high precision for proper results as Fig. 2.4 shows. Some of the graphene flakes were also transferred onto the hBN but with different substrates for the LEEM measurement. Such substrates include silicone with the native layer of the silicon oxide and Si substrate with the Au/Ti conductive layer.

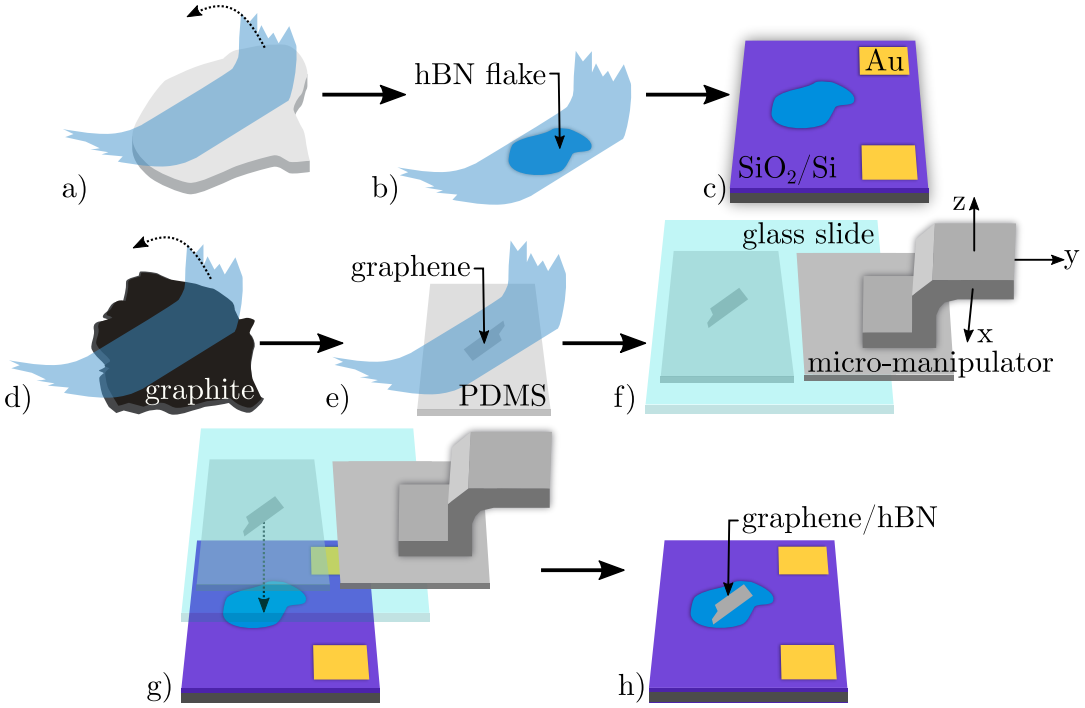

Fig. 2.3: The heterostructure creation started with a) hBN crystal exfoliation. hBN flakes are transfered from b) the adhesive blue tape c) onto the SiO_2/Si with Au pads. d) Source of graphene – graphite piece. e) Exfoliated graphene was transfered onto PDMS piece and on f) glass slide on the micro-manipulator. Using microscope and transparency of materials, g) the flakes are aligned above each other and brought into the contact. h) Heterostructure consist of graphene on the hBN flake.

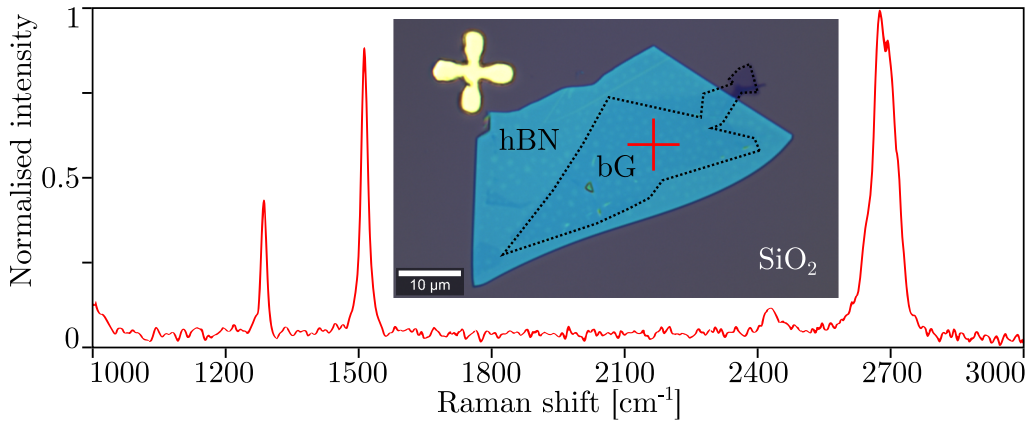

Fig. 2.4: Optical image and Raman spectrum of the sample H21 made of bi-layered graphene (bG) and hBN. Substrate is SiO_2/Si with golden marks. Red cross shows the position of spectra measurement. The hBN peak (at 1370 cm^{-1}), the G carbon peak (at 1600 cm^{-1}), and the 2D graphene peak (at 2700 cm^{-1}) are all presented in one Raman spectrum of the graphene/hBN heterostructure.

2.5 LEEM Measurements

The low energy electron microscopy (PDMS) is a powerful tool for the analysis of thin films and can be used e.g. for a precise characterization of films mutual orientation. The microscope *SPECS FE-LEEM P90* was used fom the LEEM measurements. Samples suitable for the LEEM measurements have to be conductive. Samples on the Si substrate with SiO_2 layer showed significant sample charging – no satisfying data were obtained. After that, another substrates were tried to avoid substrate charging which is incompatible with the proper measurement. The second attempt consists of the graphene/hBN structure on an n-doped conductive Si(111) substrate. The sample charging was notable right from the measurement beginning. The sample was heated up to 500 °C to get rid of an impurities and adhered water. The charging of the substrate remained and surprisingly no convenient data were measured again. In order to increase sample conductivity and get rid of the sample charging – the sample with a metallic layer was tried for the third LEEM measurements. The conductive layer included 20 nm of titanium, and 25 nm of gold. however the metal layer evaporated after heating of the sample. Multiple attempts were made, yet no diffraction data were collected. This is surprising result, we probably cannot get rid of the sample surface impurities. Some topological data were obtained as Fig. 2.5 shows.

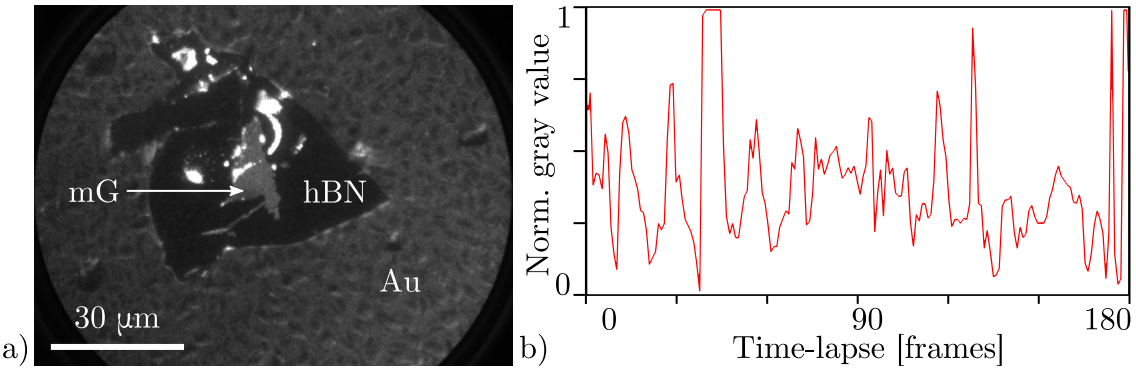

Fig. 2.5: Example of PEEM measurement of heterostructure H14 using *SPECS FE-LEEM P90* (irradiated by Hg lamp). a) the graphene mono-layer - mG on hBN flake were measured on Au platted substrate. Charging of the sample is represented with the brights. This effect is showed in time-lapse LEEM diagram b), where peaks indicates significant sample charging. Because of it, the proper measurements were not performed.

2.6 Heterostructure Contacting

The following section summaries the steps leading to graphene/hBN heterostructure connected via metallic conductive paths for the following charge carrier mobility measurements. Creating a conductive connections incorporates template preparation via spin-coating and e-beam lithography, multi-metal deposition, and later dispose of surplus material during the lift-off process.

2.6.1 Spincoating

The precisely predefined pattern is a necessary premise if one wants to contact a graphene flake. The pattern is created using a focused electron beam in an electron-sensitive film called a resist. The resists used for this work were *positive PMMA E-Beam Resists AR-P 639.04* and *AR-P 679.04*. The solvent of both resists was ethyl lactate. Resists differ in the length of the molecular chains and sensitivity to electron beam exposure. The PMMA 639.04 resist has shorter molecular chains about 50k molecules long and has a higher sensitivity to electron beam then the second resist. The PMMA 679.04 has about 950k molecules in the molecular chain. The combination of these two resists gave well-defined patterns with resolution suitable for this work.

The positive resist is a type of a resist in which the part exposed to electrons becomes soluble to a certain solution - the resist developer. The unexposed part of the positive resist stays insoluble. The effect is the opposite for the negative resist, the exposed area remains after developing. In other words, the pattern which an electron beam draws into the positive resist will be later washed away and served as a template for the metal deposition.

Before the spin coating itself, the sample was placed on the hot plate for 30 minutes at 150 °C to dehydrate sample surface (Fig 2.6 a)). This is called the pre-baking and it enhances the adhesion of the resist layer. Better results may be achieved with substrate plasma cleaning but this treatment would destroy the graphene/hBN heterostructures.

The spin coating was carried out on the *SUSS MicroTec's LabSpin 6*. The sample was placed right from the hot plate into the spin coater. The 20 ml of PMMA 639.04 were applied (Fig 2.6 b)) and coated at 2000 rps for 60 s at the acceleration of 2000 rps/s (Fig 2.6 c)). The higher rps means the thinner resist layer. During this step, the solvent of the resist evaporates and a homogeneous layer of resist stays on the sample surface. The sample was placed on the hot plate for 5 min at 150 °C after the first spin coating (Fig 2.6 d)). This step is called soft-bake, during which the resist solidifies and the rest of the resist solvent evaporates. Soft-bake is critical for good adhesion between the resist and the sample so no unwanted delamination later appears.

The sample was transferred from the hot plate into the spin coater once again for the second spinning. The PMMA 679.04 was applied (Fig 2.6 e)) and the sample was coated at 4000 rps for 60 s with the same acceleration as before (Fig 2.6 f)). The sample was placed on the hot plate after the second spin-coating for another soft-bake for 3 min at 150 °C (Fig 2.6 g)). The thickness of the final resit film should be around 390 nm according to the spin curves of the resists. This resists thickness

meets the generally recommended thickness ration of 1 : 3 between the deposited layers and resist. The conductive paths will be 100 nm thick making used resist thickness satisfying.

The whole spin coating process is summarized in the Table 2.1 and in Fig. 2.6 (a) to (g).

Tab. 2.1: The summary of the used spin coating process for the e-beam lithography. The resulting resist layer should have thickness around 390 nm.

Step #	Step Name	Parameters
1	Pre-bake	150 °C for 30 min
2	1st Spin Coating	PMMA 639.04 at 2000 rps
3	Soft-bake	150 °C for 5 min
4	2nd Spin Coating	PMMA 679.04 at 4000 rps
5	Soft-bake	150 °C for 3 min

2.6.2 Template patterning

The template patterning and selective resist exposure to focused electron beam (Fig 2.6 h)) were done on *E-beam writer RAITH 150 Two*. Used accelerating voltage was 20 kV, 60 μm condenser aperture, and 10 mm working distance. The beam was properly focused when the 2-5 nm particles were easily visible at the focusing sample. Afterward, the sample was aligned using global marks of sample coordinate system. Sample alignment has to be done carefully, the beam scanning presents sufficient power to alter resist properties. Patterning electron dose was set to be 255 μCcm^{-2} after a few testing samples.

Afterward, the samples were placed in the beaker with the resist developer - *AR 600-55* for 1 min, and in IPA for 30 (Fig 2.6 i))s. Developing subsequently showed the properly positioned pattern if all done correctly. The pattern connecting graphene flake and golden pads could be easily visible in the resist film in an optical microscope (Fig 2.6 j)). The sample was ready for the next step – the metal deposition using thermal vacuum deposition.

2.6.3 Metal Deposition and Lift-off

Metals for the conductive paths were deposited on the samples in *Electron beam evaporator BESTEC* in which the deposition material is heated up by electron bombardment (Fig 2.6 k)). The samples were rotating at the speed of 10 rpm during the whole platting to provide homogeneous metal thickness across the whole sample.

The first deposited metal was titanium which works as the adhesion layer. Titanium reacts with the oxides forming a good chemical bond and with the metals as well [83]. Since the most top layer of the substrate is SiO_2, the titanium provided suitable adhesion for the following copper layer. The main mass of the conductive path was made out of a copper because the only limited thickness of gold could be deposited in one session. The third and the last layer was gold. Au enhances the conductive properties of the paths, works as a partial anti-oxidation layer for the copper, and is a suitable material for the further bonding. The rate of depositions was monitored with the (QMC). A high rate of deposition may lead to molten metal pieces sputtering from the crucible onto the chamber walls as well as the samples. Usual rate of deposition was $\sim 1\,\text{Å}\text{s}^{-1}$. So made conductive paths were ~ 100 nm thick in total and composed of 5 nm of titanium, 75 nm of copper, and 20 nm of gold.

The deposited metals are covering everything within the line of sights like the holder with the samples. Therefore, it was necessary to remove surplus material so only conductive paths stayed. This step is called lift-off (Fig 2.6 l)) and it is the final step in the preparation of the conductive paths. The excess PMMA resist is dissolved and washed away as well as the metallic layer in acetone. Samples stayed in acetone for $8 - 10$ hours but similar results were obtained after 2 hours too.

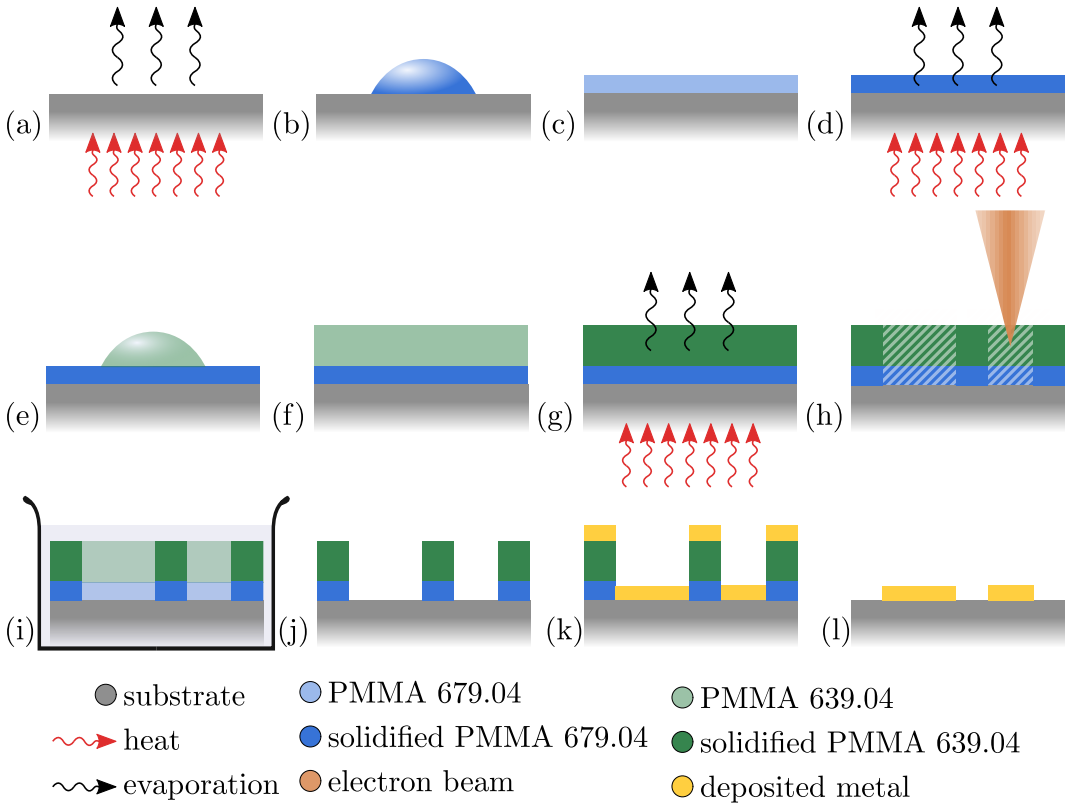

Fig. 2.6: The summary of the heterostructure contacting phase. Each picture represents one of the steps after which the graphene flake is successfully contacted and ready for conductivity measurement.
(a) Substrate is heated up and its surface is dehydrated.
(b) PMMA 639.04 is applied and
(c) coated at 2000 rps for 60 s creating 120 nm resist layer.
(d) soft-bake step to make PMMA solidified.
(e) application of PMMA 679.04
(f) coated at 4000 rps for 60 s forming additional 270 nm thick layer.
(g) second soft-bake to make resist solidified.
(h) the patterning via e-beam lithography, exposed parts loose its solidity and
(i) are washed away in the developing solution.
(j) the unexposed parts of positive resit stay on the substrate creating template for
(k) metal deposition. During the lift-off is surplus material removed and
(l) only adhered metal stays on substrate creating contacting the graphene flake.

2.7 Raman mapping

The heterostructure is exposed during each step to many factors which may cause graphene damage. Raman spectroscopy mapping was used to ensure that the device has a fine graphene layer in-between the contacts. Mapping was accomplished on *Witec Alpha 300R*. Raman mapping served for a proper determination of graphene contact geometry which is needed parameter for the mobility calculations. Samples were observed for the visual damage Fig. 2.7 a) and than mapped. The measuring conditions were similar to those for flake analysis but for time efficiency with a smaller number of accumulations. Mapped total area varied with measured heterostructure but all were done with the 0.5 μm resolution. Measured peaks were: hBN peak – Fig. 2.7 b), graphene D peak – Fig. 2.7 b), and graphene 2D peak – Fig. 2.7 c).

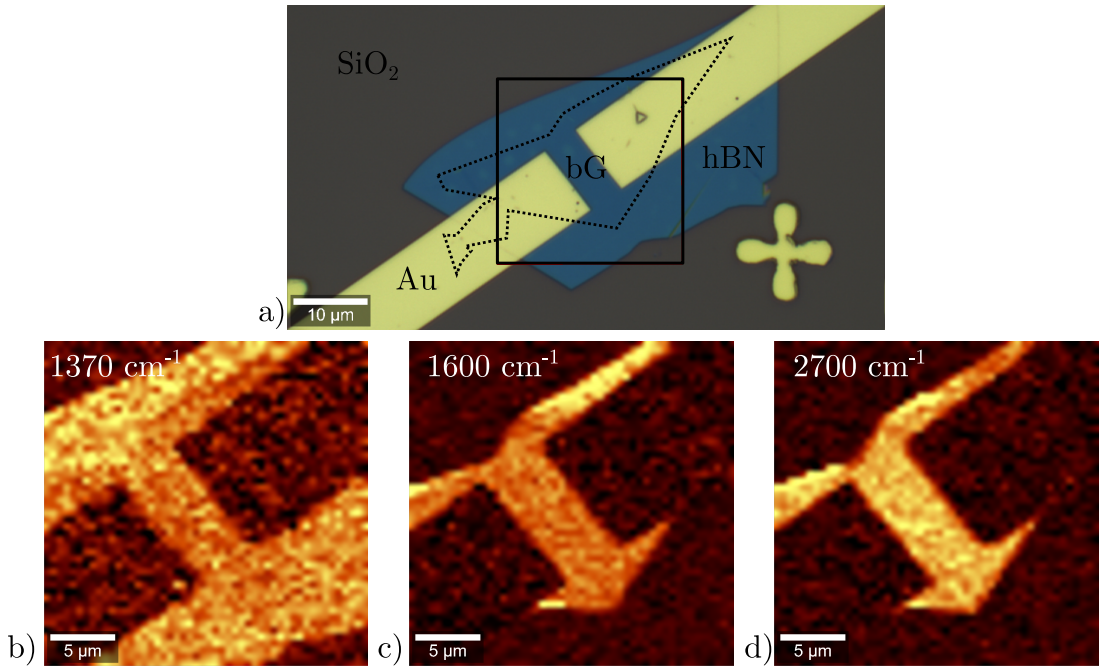

Fig. 2.7: a) Photo taken on an optical microscope with marked graphene bi-layer - bG of sample H21, conductive paths - Au, hBN flake place on SiO_2/Si substrate, and Raman mapping window – black square. Raman map showing an intensity of b) hBN peak at 1370 cm^{-1}, c) graphene G peak at 1600 cm^{-1}, d) graphene 2D peak at 2700 cm^{-1}. Scale shows 5µm.

2.8 AFM Measurement

For the exact mobility value, a thickness of the hBN flake has to be known. This was done with atomic force microscopy. hBN thickness measurements were performed on *Bruker Dimension Icon* at *Scan Asyst* mode in the air. This mode combines high-quality imaging with automatic appropriate parameter adjustments. This mode proved to be time saving sufficient option. hBN thickness of samples was measured just before the wire bonding step. The bonding could be performed only with the sample placed on the chip expander which would make AFM measurements impossible. Another reason was to check the graphene quality after the lithography phase. Samples were scanned in detail in-between the contacts and with surroundings to have a topological overview of the whole heterostructure, metal contacts, graphene flake, hBN flake, and nearby substrate surface as is depicted in Fig. 2.8 a).

The thickness of the measured samples ranged from 15 to 860 nm. The thickness of the conductive paths were (100 ± 15) nm. Measurement showed impurities, polymeric residues, and particles as the detail shows in Fig. 2.8 b).

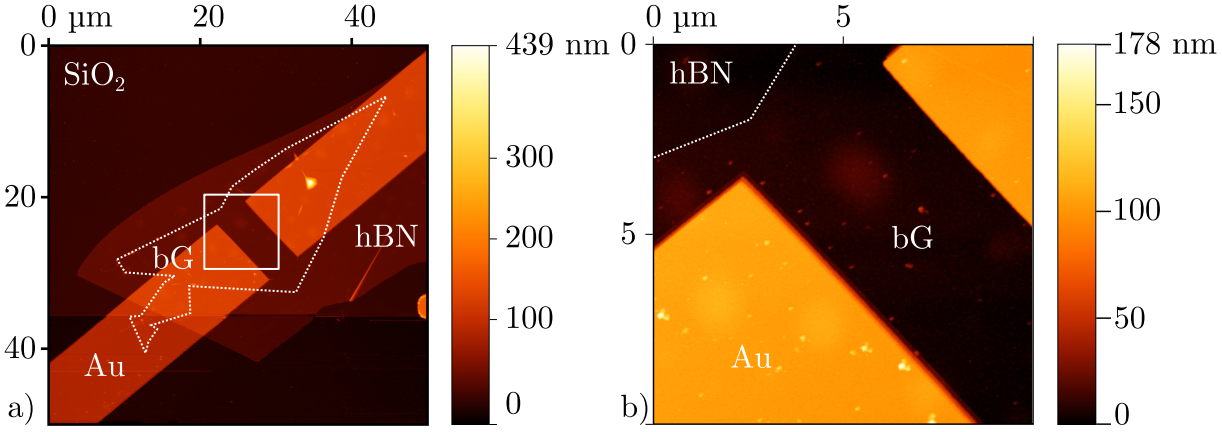

Fig. 2.8: a) AFM measurement of the heterostructure H22. Fig. shows bi-layered graphene - bG, conductive paths - Au, hBN flake, and nearby SiO_2 substrate surface. White square indicates the position of the detail scan b) showing impurities presented on the heterostructure.

2.9 Wire-bonding

The golden pads to which the graphene was connected via conductive paths are not large enough to be directly connected to the apparatus for the mobility measurements. The ceramic chip expander was used for more stable measurements and manipulation with the sample. The expander is a device with conductive pins, a resistance heating pad, and an electrode for applying the gate voltage onto the sample. All named features are placed on the ceramic plate. The sample was secured on the expander with a Kapton tape.

Wire bonder *TPT HB 16* was used for a micro-welding utilizing ultrasonic for melting down a thin golden wire to create wedge bonding between the golden pads connected to the graphene and the expander pins. To connect the sample substrate and expander – the conductive silver paint *SCP03B* was applied between the pin on the other side of the expander and the substrate. Wire-bonding was the last step of the heterostructure preparation. Prepared graphene devices (in detail in Fig. 2.9) were now ready for the conductivity measurement.

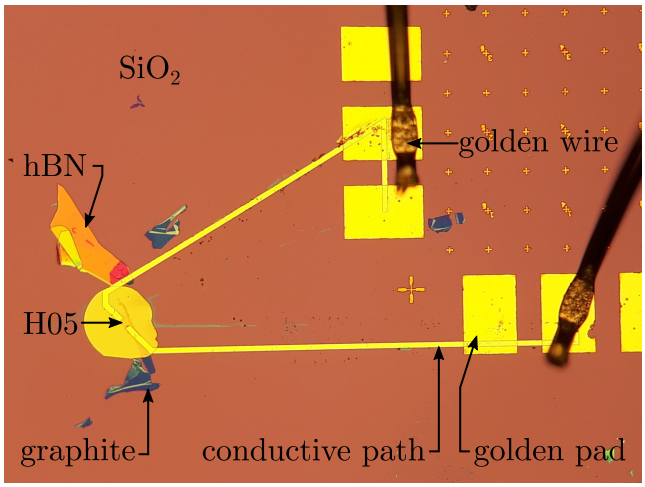

Fig. 2.9: Heterostructure H05 is connected to the chip expander pins through conductive paths, golden pads and golden wires. Fig. also shows the graphite remains after the H05 assembly, other unused hBN flake, and impurities on $Si0_2$.

2.10 Graphene Field-effect Transistor

As in the theoretical part mentioned, the charge carrier mobility is an important property of the graphene layer which is also characterizing its overall quality. Its magnitude might be measured in the graphene field-effect transistor (GFET) setup. The graphene layer of area A could be placed on the insulating layer and after applying the gate voltage V_G the charge Q accumulates in graphene as in a planar capacitor:

$$Q = CV_G = \frac{\epsilon_0 \epsilon_r A V_G}{d}, \tag{2.1}$$

where C stands for the capacitor capacitance, $\epsilon_0 = 8.854 \cdot 10^{-12}\,\mathrm{Fm}^{-1}$ is the permittivity of vacuum and ϵ_r is the relative permittivity of the dielectric medium, d is the distance between the capacitors electrodes and also the thickness of the insulating layer. As Fig. 2.10 a) shows, the used measuring setup is similar to a capacitor with two dielectrics in serial order.

The reciprocal value of the total capacitance C is then:

$$\frac{1}{C} = \frac{1}{C_1} + \frac{1}{C_2} \Rightarrow \frac{1}{C} = \frac{1}{\epsilon_0 A}\left(\frac{d_1}{\epsilon_{r1}} + \frac{d_1}{\epsilon_{r1}}\right). \tag{2.2}$$

The symbols stand for the same variables, but for the first or the second layer of dielectrics respectively. The charge in graphene Q is given by elementary charge $e = 1.602 \cdot 10^{-19}\,\mathrm{C}$ and the number of charge carriers N as:

$$Q = Ne. \tag{2.3}$$

When the gate voltage V_G changes, the concentration of the charge carrier n changes as well. The concentration n could be expressed for used graphene/hBN device using equations 2.1, 2.2, and 2.3 as:

$$n = \frac{N}{A} = \frac{\epsilon_0 \epsilon_{hBN} \epsilon_{SiO_2}}{(\epsilon_{hBN} d_{SiO_2} + \epsilon_{SiO_2} d_{hBN})} \frac{V_G}{e}. \tag{2.4}$$

Then the charge carrier mobility μ, as described in theoretical chapter 1.10, might be calculated using Drude model of electrical conduction as:

$$\sigma = en\mu, \tag{2.5}$$

where electrical conductivity σ equals the product of the charge concentration n, elemental charge e, and charge carrier mobility μ. Measured conductivity near the Dirac point should be linearly dependent on gate voltage V_G. From the slope $e\mu$ of such a relation is possible to calculate mobility μ. Electrical conductivity σ is inverse electrical resistivity ρ as:

$$\sigma = 1/\rho, \tag{2.6}$$

which could be then calculated from the resistance of graphene layer R_G as:

$$\rho = \frac{R_G W}{L}, \tag{2.7}$$

where W is the width and L length of the graphene layer covering the measuring electrodes. Determine the mobility of 2D material at the FET setup (Fig. 2.10 b)), one needs to measure the change of material resistance on the gate voltage.

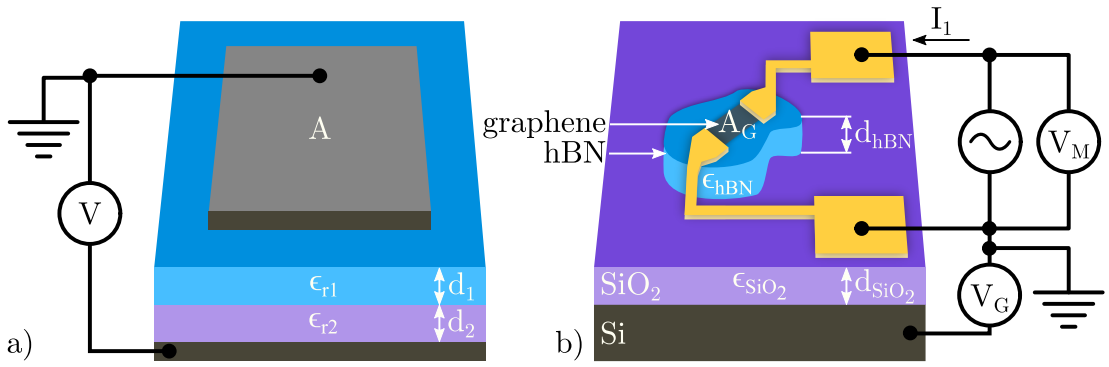

Fig. 2.10: a) Schema of the double-layered capacitor. Voltage V is applied between the top electrode of area A and the bottom electrode. Each layer has its thickness (d_1, d_1) and relative permittivity (ϵ_{r1}, ϵ_{r2}). The total capacitance of such a device is described in equation 2.2. b) Depicted graphene/hBN heterostructure setup could be also seen as the double-layered capacitor as well as the GFET. Gate voltage V_G is applied between the Si substrate and grounded graphene flake. The graphene flake is the top capacitor electrode with area A_G as well as the conductive channel of the GFET. The voltage V_M is applied between the contacts of the graphene to calculate graphene resistance R_G as the response to the change of the gate voltage V_G.

2.11 Mobility measurements

The measuring setup consisted of the power supply *Keithley 6221* (K-6221) and the lock-in amplifier *Stanford research 830* (SR-830) as Fig. 2.11 a) shows. The lock-in device was measuring the graphene resistance R_G and was connected through the resistor of $R_{10} = 10\,\mathrm{M\Omega}$, and conductive paths to the graphene layer. Thus, when an AC voltage V of frequency f is connected, an AC I_1 passes through the circuit, the magnitude of which is equal to Ohm's law as:

$$I_1 = \frac{V}{R_{10} + R_G}. \tag{2.8}$$

Since $R_{10} \gg RG$, the resistance of graphene (being in the order of hundreds of ohms) can be neglected when calculating the magnitude of the current I_1 passing through the circuit. Graphene layers are very thin and could be easily damaged by the current. The voltage for the graphene resistance measurement was set to be $V = 1\,\mathrm{V}$ thus fixing the current being $I_1 = V/R_{10} = 100\,\mathrm{nA}$. This value is safe for such a measurement. The dependence of the voltage V_M was also measured in the circuit, from which the resistance of the graphene layer R_G can be determined as:

$$R_G = \frac{V_M}{I_1}. \tag{2.9}$$

It is also necessary to know the geometry of the measured graphene contact in order to determine graphene resistivity ρ (conductivity σ) for the mobility determination.

The gate voltage V_G was applied in between the silicon substrate and heterostructure using a current supply *Keithley 6221* connected through the resistor with a resistance of $R_1 = 1\,\mathrm{M\Omega}$. For example, if the gate voltage had to be $V_G = 1\,\mathrm{V}$ the current had to be $I_2 = 1\,\mu\mathrm{A}$. The voltage across the resistor $V_G = R_1 I_2 = 1\,\mathrm{V}$ was applied to the contacts leading to the silicon substrate and heterostructure. The photograph of sample during measurement is in Fig. 2.11 b).

To summarize just described, the measured quantity was the graphene resistance R_G as a response to the change of the gate voltage V_G as Fig. 2.12 a) and b) shows. The concentration of charge carriers n was calculated using measured V_G and equations 2.1 and 2.4. The graphene conductivity σ was calculated using the graphene resistance R_G, or better the resistivity ρ according to equations 2.6 and 2.7. The dependence of the specific conductivity σ on the charge carrier concentration μ as well as on the gate voltage V_G, should be linear according to the Drude model $\sigma = en\mu$ – equation 2.5. The slope of this dependence $e\mu$ then indicates the value of the charge carrier mobility μ. The fitting of such data was performed by the least-square method.

The same measurements were also conducted at the 4-probe station *Cascade Microtech MPS 150*. The MPS 150 is more precious in data collection compare to before mentioned setup, allowing more proper mobility determination. MPS 150 allows to contact heterostructure right at the golden pads using probes on micro-manipulators. This eliminates the need for the chip expander. Unfortunately, the setup had limited gate voltage interval being $\langle -20; +20 \rangle$. The example of measured data on MPS 150 are in Fig. 2.12.

Three samples were successfully measured, namely sample H01 and H22 at the setup including Keithley 6221 and the lock-in amplifier. Another sample was successfully measured at the Cascade Microtech MPS 150 - sample H21. In overall, the mobility values ranged from 1700 to 9200 $[\mathrm{cm^2V^{-1}s^{-1}}]$ for individual measurements. Summarizing of the *experimental* chapter is further elaborated in the following chapter.

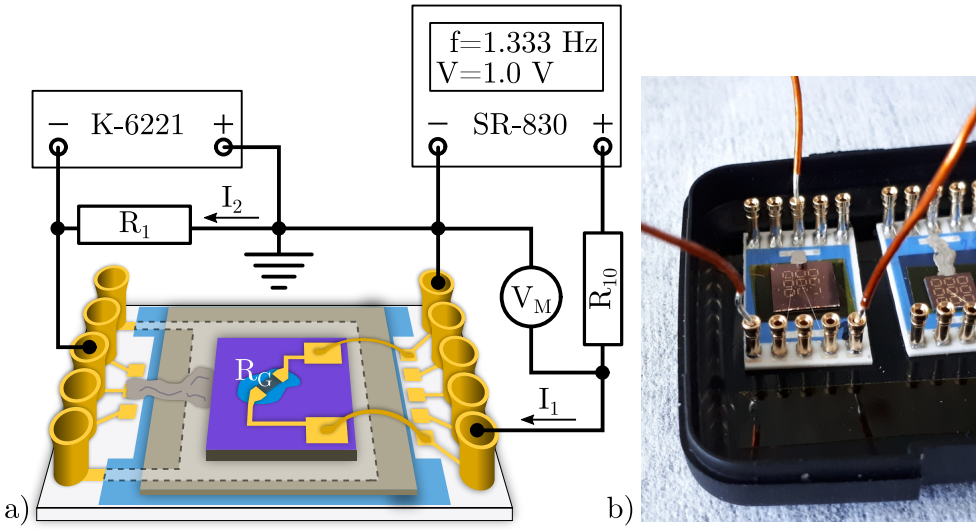

Fig. 2.11: a) Schema of measuring setup with Keithley 6221, the lock-in amplifier, and simplified sample on chip expander. b) the photography of sample H01 during measurement.

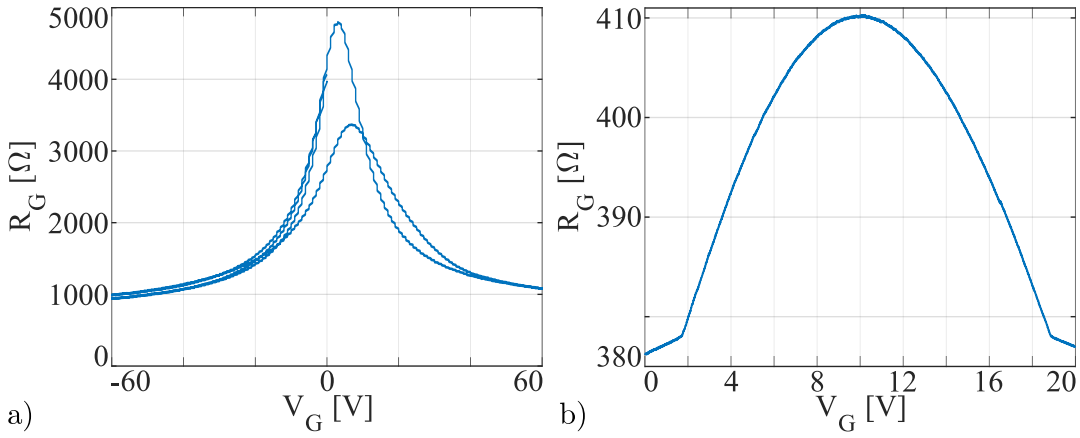

Fig. 2.12: Examples of measured data. a) Data of the sample H22 measured on the setup K-6221 + SR-830. The Position of H22 Dirac point was at 8 V. b) Data of heterostructure H21 measured at Cascade Microtech MPS 150. Dirac point position was at 10 V.

3 Results

Described **Exfoliation process** of graphene produced a good yield of graphene films, meaning mono- or bi-layered flakes. In general, on every third PDMS pieces with exfoliated flakes at least one high-quality graphene flake was found. Usually, the PDMS piece had none or multiple graphene flakes. Heating of the adhesive tape when it was in contact with PDMS piece proved to be beneficial for the exfoliation. During the heating at 70 °C, the adhesive tape softens thus enabling suitable conditions for the graphene flakes to peel-off onto the PDMS piece. The dimensions of exfoliated graphene flakes ranged from tens to hundreds of square micrometers.

The size of PDMS pieces (5×5 mm) also played an important role in the exfoliation process. When a multiple graphene layers were simultaneously found on the same PDMS piece, we had to chose only one of them for the further steps. Because only one graphene flake could be transfered onto the hBN flake during the heterostructure assembly. Larger PDMS pieces would only mean a larger number of unused graphene layers. The described hBN exfoliation proved high yield as well. Every exfoliated sample had a hBN flake that could be used for the graphene heterostructure.

Raman spectroscopy proved to be an efficient method for the graphene analysis. Measurements using the laser wavelength 532 nm had to be done with laser power ≤ 5 mW. The use of higher power of laser resulted in damaged the graphene flakes.

Described **Heterostructure assembly** proved to be precise method of van der Waal heterostructure creation. Sample heating at 85 °C created suitable conditions for the graphene transfer onto the hBN flake. The transfer without sample heating often resulted in a deterioration of contact between graphene layer and hBN flake. One in every ten graphene layers was damaged or destroyed during the assembly.

Surprisingly, the **LEEM measurement** was not successful. Three different substrates were tested to overcome the effect of substrate charging. The first substrate material was silicone with 280 nm of SiO_2, the second was conductive silicon with a native layer of SiO_2, and the third was Au/Ti platted Si wafer. All mentioned substrates exhibited a strong charging effect. No diffraction patterns were obtained, which is sign of adsorbents and impurities on sample.

The described process of **heterostructure contacting** which included spin-coating, EBL, metal deposition, lift-off, and wire-bonding demonstrated to be an accurate method for graphene contacting. As optical microscopy showed, the lithography process did not visually damage the graphene. On the other hand, the PMMA residues were observed all over the sample by optical microscopy, Raman spectroscopy and AFM.

AFM measurement showed a large number and of particles and impurities all over the heterostructure, which affirmed LEEM measurement observation. Graphene in between the metal contact showed wrinkles or encapsulated bubbles. The presence of impurities was not surprising, as the sample was not properly cleaned since the exfoliation. Due to the disproportional height of some hBN flakes and conductive paths, the electrical contact loss was found at the edge of the hBN flake. For example, heterostructure H05 was not successfully contacted, because the used hBN

flake was 860 nm tall and the conductive paths were not able to keep the contact over the such a step. The thickest successfully measured sample was H01 with hBN thickness of 305 nm. This problem could be be prevented with the AFM measurements done before the contacting phase and with a thicker layer of platted metals. Described AFM measurement was done after the heterostructure contacting phase to check the graphene quality.

In total, eight heterostructures underwent the **Mobility measurements**. Three samples were damaged during the measurement itself and two samples could not be measured due to the contact loss. The data obtained on the first setup including K-6221 and SR-830 had a wider range of gate voltage V_G which made data evaluation easier as the linear part of the measured curved was easily determined (Fig. 3.1 a)). On the other hand, the position of the Dirac points and measured data were not consistent. Nevertheless being the same measurement (as Fig. 2.12 a) shows), the shape of measured curve and the position of the Dirac points differs. The measurement inconsistency is attributed to the imperfections of the measuring system and is also reflected in the deviations mobilities.

Measurement which was done the on *Cascade Microtech MPS 150* setup had limited V_G range, the interval used for the data mobility calculation was more limited when compared to the data obtained on the first setup. This measurement also exhibited the sudden change in the measured curved. This was not observed in data from the first setup and is attributed to the imperfections of the MPS 150 measuring system. The voltage limitation is depicted in Fig. 3.1 b) where different measuring intervals can be compared. Data obtained on MPS 150 were more consistent as reflected in mobility deviations of sample H21, but the factor of limited V_G range complicated the data selection for fitting. We believe that mobility values would be higher if it was possible to measure over a wider range of the gate voltage. Higher mobility values were usually calculated from on the data outside the measuring range of the MPS 150 system.

An average of 20 values of charge carrier mobility was obtained from each sample. Successful measurements with the values of electron or hole mobility (μ_e and μ_h respectively), measuring voltage range (meas. range), and averaged voltage values of Dirac points (avg. V_D) are summarized in the table 3.1.

Tab. 3.1: The summary of the mobility measurement.

Sample	μ_e [$cm^2V^{-1}s^{-1}$]	μ_h [$cm^2V^{-1}s^{-1}$]	meas. range	avg. V_D [V]
H01	3000 ± 200	3100 ± 400	$\langle -60; +60 \rangle$	4.5
H21	1800 ± 100	2100 ± 100	$\langle -20; +20 \rangle$	11.0
H22	5900 ± 1900	6900 ± 1200	$\langle -60; +60 \rangle$	0.5

The mobility values do not reach those mentioned as the example [77] in section 1.4. But this measurements were not done at low temperatures nor vacuum chamber. The position of Dirac points were nearly always within the positive gate voltage interval. The exception was only the one measurement of sample H21. This indicates that the measured graphene layers were p-doped. Graphene p-doping could be explained by the adhered water and presence of polymeric residues. Which was confirmed by optical microscopy, Raman spectroscopy, and AFM measurement showing a large number of impurities, some of which were PMMA residues.

Still, the superior combination of the exfoliated graphene and hBN flake was confirmed in comparison to mobilities obtained at the same measuring setup on CVD graphene placed on SiO_2/Si substrate [86]. The described process of heterostructure preparation also proved to produce higher quality samples in comparison to similar work [87].

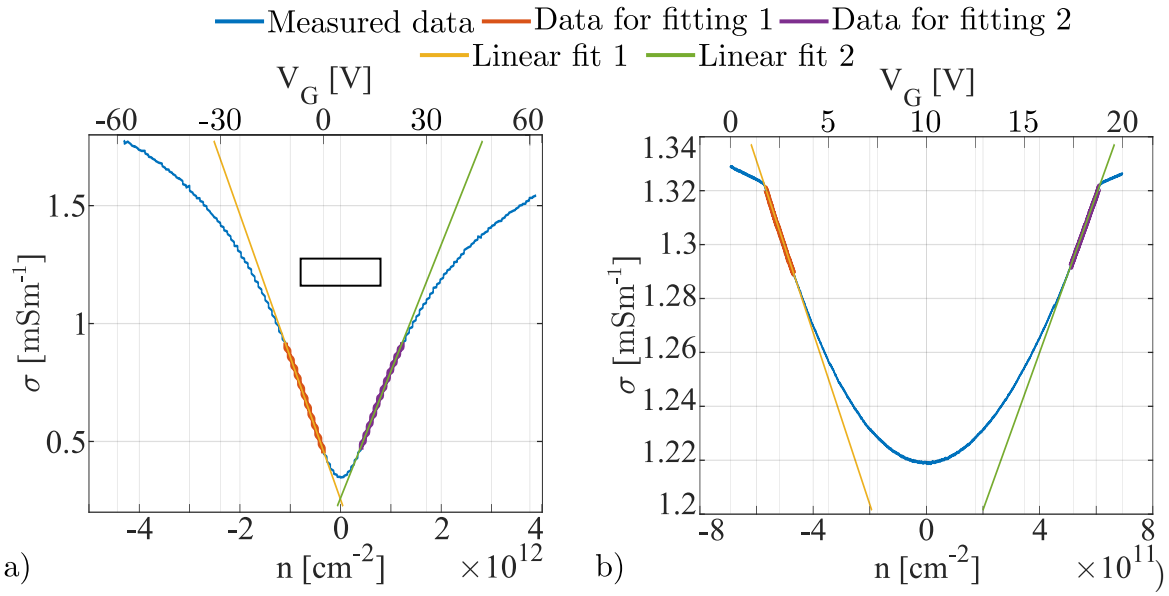

Fig. 3.1: Examples of the fitting for mobility calculation. a) Calculated data of sample H22 with highlighted data for the linear fit. Black square marks the intervals of b) similar data from sample H21. Data marked 1 and 2 correspond to hole or electron mobility respectively.

Conclusion

The goals of this masters these were:

1) Literature review of the two-dimensional materials.

2) To set an optimal process producing quality heterostructures.

3) To analyze the properties of so produced structures in an ultra-high vacuum.

The *Theoretical part* is devoted to the first goal of the thesis. The *Carbon Allotropes* section presents six different forms of carbon and also describes the similarities between the mentioned allotropes pointing out the graphene as the base of many of them. The graphene topic is further elaborated in section 1.2 *2D Materials*, which is devoted to graphene, hexagonal boron nitride, their similarities, and properties. Some of the other two-dimensional materials are mentioned like silicene, germanene, and molybdenum disulfide as well. The chemical vapor deposition, epitaxial growth, and micromechanical cleavage are discussed in detail in section 1.3 *Preparation of 2D Materials*. The methods are described along with some of their variations. The advantages and disadvantages of methods are listed as well as the quality of produced graphene. Another section – *Effect of Substrate on Graphene* – compares SiO_2 and hBN as graphene substrate, which are compared based on their influence on graphene transport properties. The remaining sections outline methods used during the *Experimental part*, their applications, and principles. Namely, atomic force microscopy, Raman spectroscopy, electron-beam lithography, electron-beam evaporation, and low-electron energy microscopy. The last section sets charge carrier mobility as a physical variable and outlines how it could be measured.

The *Experimental part* is devoted to the second and the third goal of the thesis. The heterostructure creation process starts with the preparation of graphene and hBN, the materials from which was heterostructure assembled. Graphene and hBN flakes were prepared by mechanical exfoliation. The quality of the thin films was then analyzed with Raman spectroscopy. After heterostructures assembly, the LEEM analysis was done on some samples in UHV. Surprisingly, the LEEM analysis did not produce the expected results. The samples were charging during the LEEM measurements, which is the sign of adsorbents and impurities on the sample, as was later confirmed by AFM measurements. *Heterostructure Contacting* section covers the process which delivered metal conductive paths contacting graphene/hBN heterostructure for the mobility measurements. This included spin-coating, electron-beam lithography, and metal deposition. Before the mobility measurements, two parameters had to be known – the thickness of hBN flake and the geometry of graphene contact. The hBN flake thickness was measured with AFM – section 2.8. The geometry of graphene contact was determined using the Raman spectroscopy mapping. The samples were then placed on the chip expander, auxiliary measuring devices, and contacted via thin golden wires to expander pins. Measurement of charge carrier mobility was performed at the GFET setup. The last section 2.11 *Mobility measurements* deals with data measurement, data processing, and data evaluation.

To summarize the thesis output, multiple van der Waals heterostructures made of graphene and hBN flakes were produced. The production of 2D materials was done by mechanical exfoliation which had a good yield. Heterostructures were pre-

ciously assembled and contacted. Raman spectroscopy and AFM were successfully used to analyzed the graphene/hBN structure. The charge carrier mobility measurements were accomplished on two measuring systems. Obtained values of mobility demonstrated excelling transport properties of the exfoliated graphene over the CVD prepared graphene thus proving the described creation process as suitable for the preparation of quality heterostructures.

Bibliography

[1] Collins, A. T. The optical and electronic properties of semiconducting diamond. *Philosophical Transactions of the Royal Society of London. Series A: Physical and Engineering Sciences* **342**, 233–244 (1993).

[2] Kroto, H. W., Heath, J. R., O'Brien, S. C., Curl, R. F. & Smalley, R. E. C60: Buckminsterfullerene. *Nature* **318**, 162–163 (1985).

[3] Chen, Z. *et al.* Is c_{60} buckminsterfullerene aromatic? *Physical Chemistry Chemical Physics* **14**, 14886–14891 (2012).

[4] Hirsch, A. & Brettreich, M. *Fullerenes: chemistry and reactions* (John Wiley & Sons, 2006).

[5] Blank, V. *et al.* Ultrahard and superhard carbon phases produced from c_{60} by heating at high pressure: structural and raman studies. *Physics Letters A* **205**, 208–216 (1995).

[6] Sundqvist, B. Fullerenes under high pressures. *Advances in Physics* **48**, 1–134 (1999).

[7] Lalwani, G. & Sitharaman, B. Multifunctional fullerene-and metallofullerene-based nanobiomaterials. *Nano Life* **3**, 1342003 (2013).

[8] Shi, L. *et al.* Confined linear carbon chains as a route to bulk carbyne. *Nature Materials* **15**, 634–639 (2016).

[9] NuLi, Y. *et al.* Carbyne polysulfide as a novel cathode material for rechargeable magnesium batteries. *The Scientific World Journal* (2014).

[10] Alred, J. M., Gupta, N., Liu, M., Zhang, Z. & Yakobson, B. I. Mechanics of materials creation: nanotubes, graphene, carbyne, borophenes. *Procedia IUTAM* **21**, 17–24 (2017).

[11] Oberlin, A., Endo, M. & Koyama, T. Filamentous growth of carbon through benzene decomposition. *Journal of Crystal Growth* **32**, 335–349 (1976).

[12] Zhang, R. *et al.* Growth of half-meter long carbon nanotubes based on schulz–flory distribution. *ACS Nano* **7**, 6156–6161 (2013).

[13] Peng, B. *et al.* Measurements of near-ultimate strength for multiwalled carbon nanotubes and irradiation-induced crosslinking improvements. *Nature Nanotechnology* **3**, 626–631 (2008).

[14] Han, Z. & Fina, A. Thermal conductivity of carbon nanotubes and their polymer nanocomposites: A review. *Progress in Polymer Science* **36**, 914–944 (2011).

[15] Li, W. *et al.* Large-scale synthesis of aligned carbon nanotubes. *Science* **274**, 1701–1703 (1996).

[16] Nikolaev, P. *et al.* Gas-phase catalytic growth of single-walled carbon nanotubes from carbon monoxide. *Chemical Physics Letters* **313**, 91–97 (1999).

[17] Kharissova, O., Castañón, M. G., Hernandez Pinero, J., Méndez, U. O. & Kharisov, B. Fast production method of fe-filled carbon nanotubes. *Mechanics of Advanced Materials and Structures* **16**, 63–68 (2009).

[18] Journet, C. *et al.* Large-scale production of single-walled carbon nanotubes by the electric-arc technique. *Nature* **388**, 756–758 (1997).

[19] Narayan, J. & Bhaumik, A. Research update: direct conversion of amorphous carbon into diamond at ambient pressures and temperatures in air. *APL Materials* **3**, 100702 (2015).

[20] Kim, T., Lee, J. & Lee, K.-H. Full graphitization of amorphous carbon by microwave heating. *RSC Advances* **6**, 24667–24674 (2016).

[21] Sinitsa, A. S., Lebedeva, I. V., Popov, A. M. & Knizhnik, A. A. Transformation of amorphous carbon clusters to fullerenes. *The Journal of Physical Chemistry C* **121**, 13396–13404 (2017).

[22] Zheng, M. *et al.* Metal-catalyzed crystallization of amorphous carbon to graphene. *Applied Physics Letters* **96**, 063110 (2010).

[23] Novoselov, K. S. *et al.* Electric field effect in atomically thin carbon films. *Science* **306**, 666–669 (2004).

[24] Rutherford, R. B. & Dudman, R. L. Ultra-thin flexible expanded graphite heating element (2003). US Patent 6,667,100.

[25] Boehm, H., Clauss, A., Fischer, G. & Hofmann, U. Adsorption behaviors of extremely thin carbon foils anorg. *Journal of Inorganic and General Chemistry* **316**, 119–127 (1962).

[26] Ruess, G. & Vogt, F. Höchstlamellarer kohlenstoff aus graphitoxyhydroxyd. *Monatshefte für Chemie und verwandte Teile anderer Wissenschaften* **78**, 222–242 (1948).

[27] Charlier, J.-C., Eklund, P., Zhu, J. & Ferrari, A. Electron and phonon properties of graphene: their relationship with carbon nanotubes. In *Carbon Nanotubes*, 673–709 (Springer, 2007).

[28] Neto, A. C., Guinea, F., Peres, N. M., Novoselov, K. S. & Geim, A. K. The electronic properties of graphene. *Reviews of Modern Physics* **81**, 109 (2009).

[29] Lee, C., Wei, X., Kysar, J. W. & Hone, J. Measurement of the elastic properties and intrinsic strength of monolayer graphene. *Science* **321**, 385–388 (2008).

[30] Bae, S. *et al.* Roll-to-roll production of 30-inch graphene films for transparent electrodes. *Nature Nanotechnology* **5**, 574–578 (2010).

[31] Pop, E., Varshney, V. & Roy, A. K. Thermal properties of graphene: Fundamentals and applications. *MRS Bulletin* **37**, 1273–1281 (2012).

[32] Chen, S. *et al.* Raman measurements of thermal transport in suspended monolayer graphene of variable sizes in vacuum and gaseous environments. *ACS Nano* **5**, 321–328 (2011).

[33] Ghosh, d. *et al.* Extremely high thermal conductivity of graphene: Prospects for thermal management applications in nanoelectronic circuits. *Applied Physics Letters* **92**, 151911 (2008).

[34] Seol, J. H. *et al.* Two-dimensional phonon transport in supported graphene. *Science* **328**, 213–216 (2010).

[35] Sharma, R., Baik, J. H., Perera, C. J. & Strano, M. S. Anomalously large reactivity of single graphene layers and edges toward electron transfer chemistries. *Nano Letters* **10**, 398–405 (2010).

[36] He, H. & Gao, C. General approach to individually dispersed, highly soluble, and conductive graphene nanosheets functionalized by nitrene chemistry. *Chemistry of Materials* **22**, 5054–5064 (2010).

[37] Mayorov, A. S. *et al.* Micrometer-scale ballistic transport in encapsulated graphene at room temperature. *Nano Letters* **11**, 2396–2399 (2011).

[38] Bolotin, K. I. *et al.* Ultrahigh electron mobility in suspended graphene. *Solid State Communications* **146**, 351–355 (2008).

[39] Morozov, S. *et al.* Giant intrinsic carrier mobilities in graphene and its bilayer. *Physical Review Letters* **100**, 016602 (2008).

[40] Kulkarni, D. D., Choi, I., Singamaneni, S. S. & Tsukruk, V. V. Graphene oxide-polyelectrolyte nanomembranes. *ACS Nano* **4**, 4667–4676 (2010).

[41] Huang, C., Hao, Z., Qi, T., Pan, Y. & Zhao, X. An integrated flexible and reusable graphene field effect transistor nanosensor for monitoring glucose. *Journal of Materiomics* **6**, 308–314 (2020).

[42] Urban, F., Lupina, G., Grillo, A., Martucciello, N. & Di Bartolomeo, A. Contact resistance and mobility in back-gate graphene transistors. *Nano Express* **1**, 010001 (2020).

[43] Bareza, N., Gopalan, K. K., Alani, R., Paulillo, B. & Pruneri, V. Mid-infrared gas sensing using graphene plasmons tuned by reversible chemical doping. *ACS Photonics* **7**, 879–884 (2020).

[44] Lee, J.-S. *et al.* Layer-by-layer assembled charge-trap memory devices with adjustable electronic properties. *Nature Nanotechnology* **2**, 790–795 (2007).

[45] Wang, S., Pu, J., Chan, D. S., Cho, B. J. & Loh, K. P. Wide memory window in graphene oxide charge storage nodes. *Applied Physics Letters* **96**, 143109 (2010).

[46] Böhm, S. Graphene against corrosion. *Nature Nanotechnology* **9**, 741–742 (2014).

[47] Yoon, J. *et al.* Superflexible, high-efficiency perovskite solar cells utilizing graphene electrodes: towards future foldable power sources. *Energy & Environmental Science* **10**, 337–345 (2017).

[48] Zhou, C. & Szpunar, J. A. Hydrogen storage performance in pd/graphene nanocomposites. *ACS Applied Materials &Interfaces* **8**, 25933–25940 (2016).

[49] Han, Y., Xu, Z. & Gao, C. Ultrathin graphene nanofiltration membrane for water purification. *Advanced Functional Materials* **23**, 3693–3700 (2013).

[50] Chen, H. *et al.* Ultrafast all-climate aluminum-graphene battery with quarter-million cycle life. *Science Advances* **3**, 7233 (2017).

[51] Giovannetti, G., Khomyakov, P. A., Brocks, G., Kelly, P. J. & Van Den Brink, J. Substrate-induced band gap in graphene on hexagonal boron nitride: Ab initio density functional calculations. *Physical Review B* **76**, 073103 (2007).

[52] Falin, A. *et al.* Mechanical properties of atomically thin boron nitride and the role of interlayer interactions. *Nature Communications* **8**, 1–9 (2017).

[53] Li, L. H., Cervenka, J., Watanabe, K., Taniguchi, T. & Chen, Y. Strong oxidation resistance of atomically thin boron nitride nanosheets. *ACS Nano* **8**, 1457–1462 (2014).

[54] Li, L. H., Xing, T., Chen, Y. & Jones, R. Boron nitride nanosheets for metal protection. *Advanced Materials Interfaces* **1**, 1300132 (2014).

[55] Dean, C. R. *et al.* Boron nitride substrates for high-quality graphene electronics. *Nature Nanotechnology* **5**, 722–726 (2010).

[56] Zhang, K., Feng, Y., Wang, F., Yang, Z. & Wang, J. Two dimensional hexagonal boron nitride (2d-hbn): synthesis, properties and applications. *Journal of Materials Chemistry C* **5**, 11992–12022 (2017).

[57] Guzmán-Verri, G. G. & Voon, L. L. Y. Electronic structure of silicon-based nanostructures. *Physical Review B* **76**, 075131 (2007).

[58] Li, L. *et al.* Buckled germanene formation on pt (111). *Advanced Materials* **26**, 4820–4824 (2014).

[59] Ni, Z. *et al.* Tunable bandgap in silicene and germanene. *Nano Letters* **12**, 113–118 (2012).

[60] He, Z. & Que, W. Molybdenum disulfide nanomaterials: structures, properties, synthesis and recent progress on hydrogen evolution reaction. *Applied Materials Today* **3**, 23–56 (2016).

[61] Roy, T. *et al.* Field-effect transistors built from all two-dimensional material components. *ACS Nano* **8**, 6259–6264 (2014).

[62] Li, X. *et al.* Large-area synthesis of high-quality and uniform graphene films on copper foils. *Science* **324**, 1312–1314 (2009).

[63] De Arco, L. G., Zhang, Y., Kumar, A. & Zhou, C. Synthesis, transfer, and devices of single-and few-layer graphene by chemical vapor deposition. *IEEE Transactions on Nanotechnology* **8**, 135–138 (2009).

[64] Shi, Q. *et al.* Substrate developments for the chemical vapor deposition synthesis of graphene. *Advanced Materials Interfaces* 1902024 (2020).

[65] Banszerus, L. *et al.* Ultrahigh-mobility graphene devices from chemical vapor deposition on reusable copper. *Science Advances* **1**, e1500222 (2015).

[66] Kobayashi, T. *et al.* Production of a 100-m-long high-quality graphene transparent conductive film by roll-to-roll chemical vapor deposition and transfer process. *Applied Physics Letters* **102**, 023112 (2013).

[67] Vesselinov, M. I. *Crystal growth for beginners: Fundamentals of nucleation, crystal growth and epitaxy* (World scientific, 2016).

[68] Chen, T.-A. *et al.* Wafer-scale single-crystal hexagonal boron nitride monolayers on cu (111). *Nature* **579**, 219–223 (2020).

[69] Yang, W. *et al.* Epitaxial growth of single-domain graphene on hexagonal boron nitride. *Nature Materials* **12**, 792–797 (2013).

[70] Du, W., Jiang, X. & Zhu, L. From graphite to graphene: direct liquid-phase exfoliation of graphite to produce single-and few-layered pristine graphene. *Journal of Materials Chemistry A* **1**, 10592–10606 (2013).

[71] Hummers Jr, W. S. & Offeman, R. E. Preparation of graphitic oxide. *Journal of the American Chemical Society* **80**, 1339–1339 (1958).

[72] Fan, X., Chang, D. W., Chen, X., Baek, J.-B. & Dai, L. Functionalized graphene nanoplatelets from ball milling for energy applications. *Current Opinion in Chemical Engineering* **11**, 52–58 (2016).

[73] Su, C.-Y. *et al.* High-quality thin graphene films from fast electrochemical exfoliation. *ACS Nano* **5**, 2332–2339 (2011).

[74] Huang, Y. *et al.* Reliable exfoliation of large-area high-quality flakes of graphene and other two-dimensional materials. *ACS Nano* **9**, 10612–10620 (2015).

[75] Dorgan, V. E., Bae, M.-H. & Pop, E. Mobility and saturation velocity in graphene on sio 2. *Applied Physics Letters* **97**, 082112 (2010).

[76] Wang, J., Ma, F. & Sun, M. Graphene, hexagonal boron nitride, and their heterostructures: properties and applications. *RSC Advances* **7**, 16801–16822 (2017).

[77] Burson, K. M. *et al.* Direct imaging of charged impurity density in common graphene substrates. *Nano Letters* **13**, 3576–3580 (2013).

[78] Voigtländer, B. *Scanning probe microscopy: Atomic force microscopy and scanning tunneling microscopy* (Springer, 2015).

[79] Tan, P.-H. *Raman Spectroscopy of Two-dimensional Materials*, vol. 276 (Springer, 2018).

[80] Ferrari, A. C. *et al.* Raman spectrum of graphene and graphene layers. *Physical Review Letters* **97**, 187401 (2006).

[81] Stenger, I. *et al.* Low frequency raman spectroscopy of few-atomic-layer thick hbn crystals. *2D Materials* **4**, 031003 (2017).

[82] Yao, N. & Wang, Z. L. *Handbook of microscopy for nanotechnology* (Springer, 2005).

[83] Weihs, T. Handbook of thin film process technology. *ed DA Glocker, SI Shah, Institute of Physics, Bristol, UK F* **7** (1998).

[84] Bauer, E. *Surface microscopy with low energy electrons*, vol. 23 (Springer, 2014).

[85] Hawkes, P. W. & Spence, J. C. *Springer Handbook of Microscopy* (Springer Nature, 2019).

[86] J., T. *Graphene Transfer Methods For High Quality Graphene Field Effect Transistors*. Master's thesis, Brno University of Technology (2018). Bachelor's Thesis.

[87] I., M. *Fabrication and Characterization of Two Dimensional Heterostructures*. Master's thesis, Brno University of Technology (2018). Master's Thesis.

List of abbreviations

PDMS	Polydimethylsiloxane
CVD	Chemical vapor deposition
UHV	Ultra high vacuum
GFET	Graphene field-effected tranzistor
WD	Working distance
IPA	Isopropyl alcohol
IPA	Hexagonal boron nitride
hBN	Hexagonal nanotubes
CNTs	Carbon nanotubes
CVD	Chemical vapor deposition
MC	Mechanical cleavage
EBL	Electron beam lithography
LEEM	Low electron energy microscopy
LEED	Low electron energy diffraction
SEM	Scanning electron microscope
mG	Mono-layered graphene
bG	Bi-layered graphene